Universitat Autònoma de Barcelona

Chemical Transducers Group (GTQ)

Institut de Microelectrònica de Barcelona (IMB-CNM)

Consejo Superior de Investigaciones Científicas (CSIC)

Programa de Doctorat en Física
Thesis submitted to obtain the degree of Doctor in Philosophy

---

Living Photonics: Lab-on-a-chip technologies for light coupling into biological cells

Doctoral Dissertation of:
Tobias Nils Ackermann

Supervisors:
Dr. Andreu Llobera Adàn

and
Dr. Xavier Muñoz Berbel

Tutor:
Prof. Dr. Verònica Ahufinger

September 2017

4.5 Monitoring of biofilm colonization: Dynamic conditions.

In order to assimilate the real situation of a water distribution pipe a bit farther, the next logical step in the technological development was to design a complete PhLoC comprising integrated optics and a fluidic channel for the study of surface colonisation under flow conditions.

4.5.1 Experimental design and Simulation

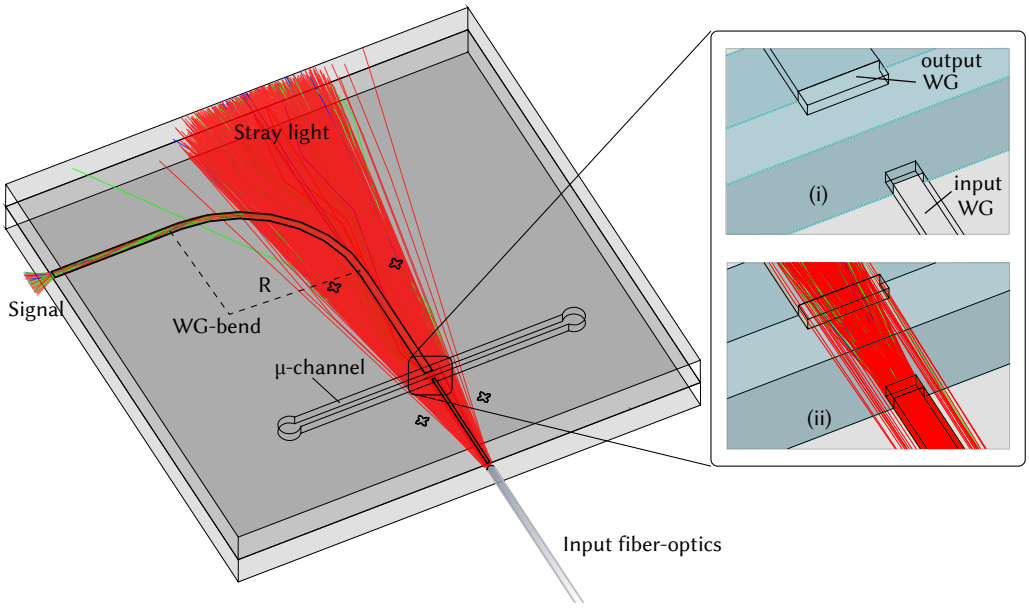

Figure 4.23: 3D- representation and simulation of the proposed PhLoC. Red, green and blue lines are the result of a ray tracing simulation of the chip using TracePro. Inset (i) shows a detail of the area where the two waveguides are interrupted by the fluidic channel without rays, inset (ii) the same area plotting only rays coupled to the WG-bend and reaching the designed output (Signal).

Fig. 4.23 shows a 3D-representation of the first generation PhLoC design, whose footprint was already introduced for convenience in the section concerned with its fabrication (Fig. 4.23). As described previously, the PhLoC comprises a straight input and a 90° bent output waveguide interrupted by a fluidic channel, which is perpendicular to direction of light propagation. The architecture was designed to be compatible with the physical CWI presented in the previous chapter (Section ??). The ray tracing simulation displayed on the right was again performed using TracePro. From there we gather that as expected, most of the input light not coupled into the straight input waveguide is lost in forward direction as stray light, while the part of light

coupled across the fluidic channel into the output WG is guided along the bend to the output plane (signal) and thus decoupled from the stray light (noise).

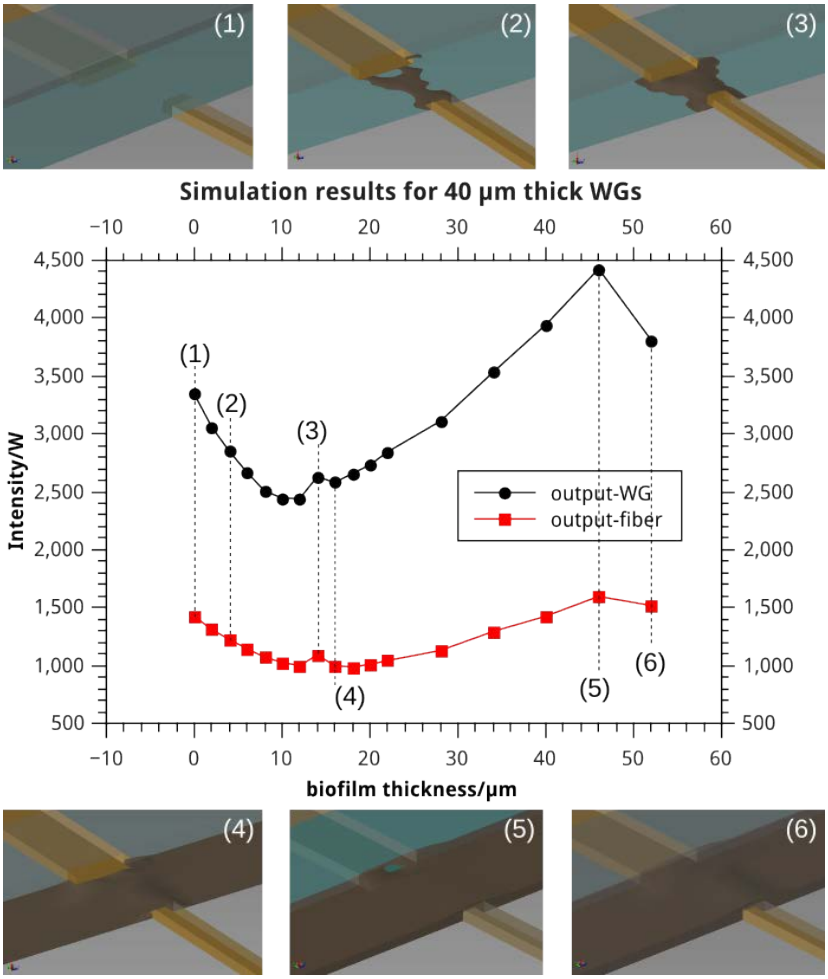

Figure 4.24: Ray tracing simulations performed with TracPro to explore the influence of a vastly simplified model biofilm with homogeneous refractive index throughout its bulk growing preferentially in the "modified" surface area between the waveguides on the transmission characteristics of the interrupted waveguides displayed in the previous figure ??.

Based on this design, a biofilm model was implemented in TracePro to optically simulate preferential adhesion and biofilm formation in the µ-channel region between the two waveguides (shown in detail in the insets of Fig. 4.23). Assuming we can reproduce the micro-patterns from the previous section inside the µ-channels, locally accelerated biofilm formation may progress as in the model shown at different stages in Fig. 4.24. The biofilm model implemented in TracePro was optically vastly simplified. For this initial assessment we supposed that the extracellular matrix and the bacteria together form a biomaterial with locally homogeneous average refractive index of $n = 1.39$. The simulated situation may be approximated experimentally by applying

a laser-engraving to the PMMA bottom layers of the PhLoC prior to the 'sealing' or 'bonding' process and according to the process parameters previously established as optimal for adhesion promotion.

4.5.2 Bacterial culture

In order to be able to be able to use the previously presented characterisation of surface colonisation kinetics on PMMA and PMMA with SU-8, Pseudomona putida (*P. putida*) was chosen as model bacterium for this experiment. As before, bacterial suspensions were grown overnight in minimum medium AB (MMAB) supplemented with 0.2% glucose (w/v) at 30°C in a thermal bath agitator. Overnight cultures were then centrifuged and re-suspended in MMAB. The optical density of the final suspension was adjusted by dilution with deionised water to 1 absorbance unit (A.U.) at 550 nm with MMAB, which corresponded to a bacterial concentration around 10^8 colony forming units per mL (CFU/mL). The resulting bacterial suspension was kept without adding further nutrients for the length of the experiment and circulated in a closed circuit from the culture flask through the PhLoC's µ-channel and back.

4.5.3 Setup

Fig.4.25 (a) depicts the setup used for the monitoring in dynamic conditions. Instead of the white LED used in the previous section, we employed a halogen lamp (HL-2000, Ocean Optics, Inc.) in this case in order to achieve a more evenly distributed input intensity along with the Ocean Optics QE 65000 photospectrometer for detection. Both devices were coupled in order to open the shutter of the light source only at the times of measurement. The latter mechanism also served the purpose of enabling real-time ambient light correction, which was accomplished via the custom LabVIEW software interface presented in section 3.3.2. Optical connections were again established using a CWI as the one presented in Chapter 3 using 200/230 µm SMA-connected fiber-optics. For fluidic connections however, an additional piece was added in form of the lid depicted schematically in Fig. 4.25 (b), comprising LUER syringe connectors as standardised fluidic interconnects in a distance adapted to the separation of the fluidic inlets of the first generation PhLoC and a piece of PDMS acting as a toric joint between lid and PhLoC. A photograph of the fully assembled CWI is shown in Fig. 4.25 (c). After successfully testing the fluidic connections by circulating water during one week at average flow-rate of 1.25 mL min^{-1}, the re-suspended and concentration adjusted overnight culture was connected for perpetual circulation through the µ-channel. The initial water circulation also served the purpose of gaining ample reference spectra for the optical monitoring.

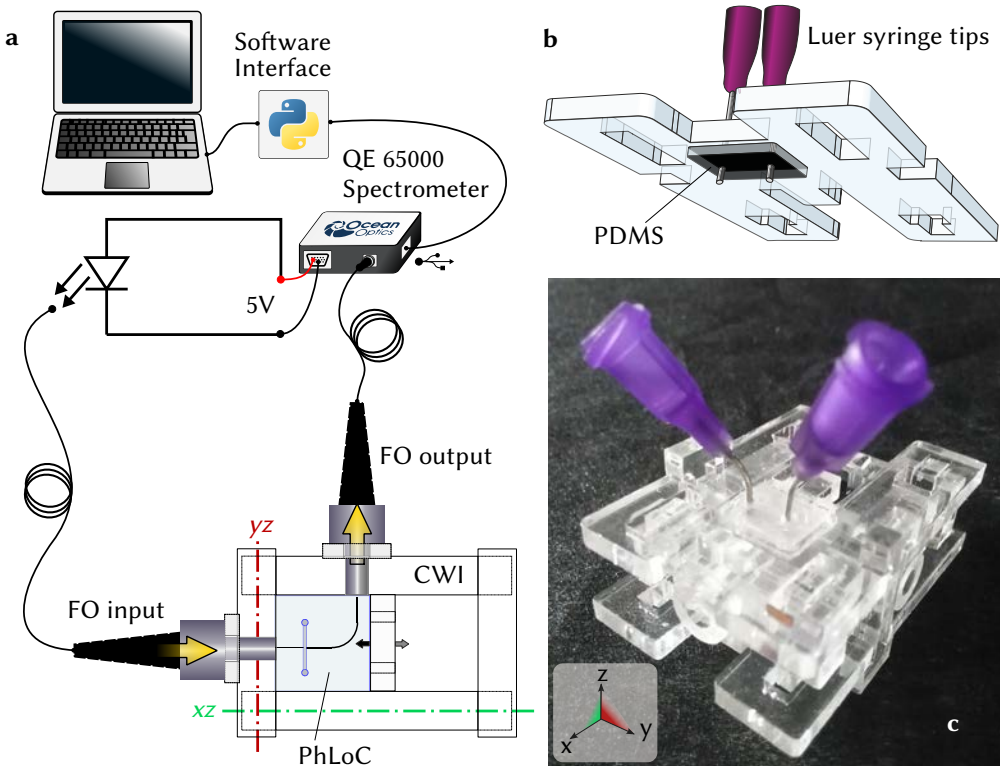

Figure 4.25: (a) Schematic of the experimental setup in terms of the optical measurement. (b) Schematic representation of additional lid for the chip-to-world interface (CWI) providing a PDMS based thoric junction and Luer syringe tips for standardised fluidic connections to and from the bacterial culture flask. Liquid was pumped in a closed circuit from the flask to the PhLoC and back. (c) Photograph of the modified CWI used in the dynamic experiment with the first generation PhLoC.

4.5.4 Results and discussion

In the results shown in Fig 4.26, the spectral response of the biofilm starts off with the same scattering pattern as observed in static conditions. Over time, again the steepness of the scattering dependence decreases. On the other hand, in this case the absolute values over time are theoretically comparable as due to the stable setup no re-adjustments of the optical connections could interfere with the input light intensity. An overall increasing offset of the absorbance spectra with timewas registered, until at the last presented time of 7680 h (= 5.3 days), the spectral response grew completely flat, but maintained the offset at long wavelengths of the prior measurement. The absorbance over time data plotted in the graph on the bottom is consistent with the tendency observed in the simplified simulation model shown in Fig.4.24 up until stage (3), where TIR effects take over and cause the overall transmitted intensity to increase again as opposed to the initial scattering by small patches of not interconnected bacterial colonies.

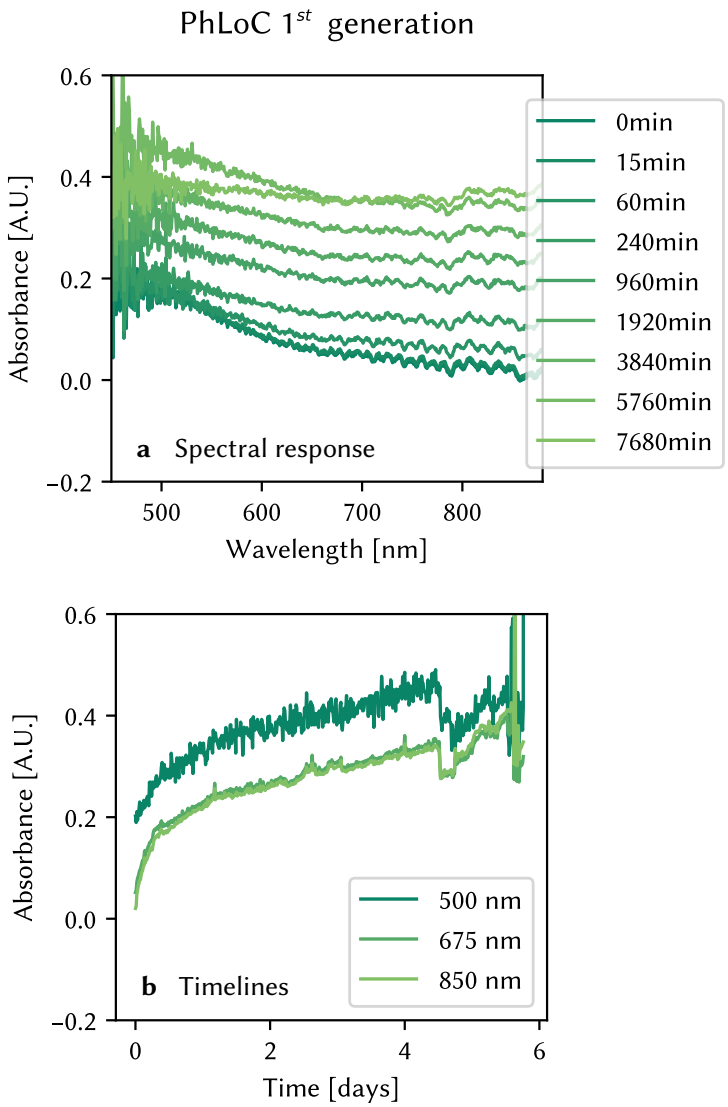

Figure 4.26: Preliminary results obtained in flow conditions with P. putida circulating through the chip. (Left) Self referenced Absorbance spectra at different points in time. (Right) Absorbance values at two concrete wavelength values over time.

After approximately 4.5 days, and well before the last presented spectral response deviating from the previous tendency, the fluidic connection failed at the (PDMS) toric joint, probably as an effect of the building back-pressure with increasing bacterial growth and obstrusion of fluid flow inside the µ-channel inside the PhLoC. The effect on the absorbance signal can be clearly identified as an abrupt drop, which seems to recover subsequently, yet does so less rapidly at shorter wavelength (compare the 500 nm signal to the ones at 675 nm and 850 nm), resulting in the in-congruent spectral response at 7680 h. The latter suggests that the gross of biofilm attached in the sensing region may have been removed during the leak, thus removing the scat-

tering pattern. Alternatively, and given the overall absorbance offset maintained in the process, a big enough aggregate with sufficiently homogeneous average refractive index to display reduced scattering efficiency from another part of the fluidic circuit(e. g. the culture flask) may have entered the sensing area and given rise to the altered spectral response. Without real-time visual feedback however, further speculation on the subject are futile.

4.6 Conclusions

Three approaches for the integration of waveguides into a thermoplastic PMMA substrate have been demonstrated, namely embedding of fiber-optics segments, and the encapsulation of SU-8 waveguides using direct photolithography and waveguide transfer. The chemical treatments involved development proofed to be problematic using PMMA as the substrate. The transfer of SU-8 microstructures from a Si substrate to the thermoplastic was demonstrated as a more robust technique for waveguide encapsulation, leaving the Si wafer bare and intact after the transfer. Further it was shown how complete encapsulation can be achieved by bonding to a subsequent PMMA layer and fusing the borders to a smooth edge with a CO_2 laser. The latter step combines the robust sealing of the microfluidic channel with the entire back-end processing necessary to end up with a fully functional photonic lab-on-a-chip, as has been demonstrated through the optical calibration. In each of the proposed fabrication schemes, conventional elements have been combined with CO_2-laser processing of the thermoplastic in order to end up with a functional device for the optical monitorisation of surface colonisation by bacterial biofilms. The latter process on the concrete structural materials has been studied thoroughly by conventional confocal microscopy as a basis for the interpretation of spectral obtained in the subsequent optical measurements. It could be shown that by locally modifying the PMMA surface via laser-engraving, enhanced bacterial adhesion as compared to unmodified surfaces can be achieved, resulting in significantly thicker and more dense bacterial layers in the modified regions. The benefits of the latter effect were explored by incorporating the optimum engraving conditions into the respective fabrication schemes as a substrate pre-treatment and evaluated in the subsequent optical measurements. In static as well as dynamic conditions, biofilm monitoring yielded spectral data consistent with bacterial colonisation. The acceleration of bacterial adhesion in the initial phase of surface colonisation promoted by localised surface modification could be confirmed by spectral analysis in the case of the static culture conditions. Also, specific absorption bands were observed from GFP expressing *E. coli*. In dynamic conditions inside a closed µ-channel, absolute absorbance values could be compared and were found to be consistent with ray-tracing simulations when considering unconnected but optically homogeneous

aggregates of bacteria. Using *P. putida* as model bacterium, no specific absorption bands were observed. In the experimental application of the fabricated PhLoCs to biofilm monitorisation, the physical as well the software interfacing described in chapter 3 could be employed beneficially, providing stable and repeatable optical connections and automated signal acquisition over several days. A future implementation of the second generation PhLoC using a thin bottom layer and applying a surface modification to one of the sensing sites may enable real-time visual feedback for benchmarking and offer an additional reference measurement for an estimation of the effect of the laser-induced surface modifications in dynamic conditions.

Low refractive index PhLoCs for light confinement in cell monolayers 5

The following chapter encompasses the efforts directed towards the implementation of (mammalian) cell monolayers as living photonic components. This part was in many aspects the most challenging one and is therefore the concluding chapter of this thesis.

5.1 Introduction

As already stated before, the concept of living photonics suggests a host of possibilities in terms of contactless and minimal invasive monitoring of biological processes. Mammalian cell monolayers have a long history as models for drug development and disease factors. Further, since the introduction of PDMS for the construction of microfluidic channels *on-chip* cell cultures have become increasingly interesting for scientists, as the LoC environment provides unprecedented control of the cells' micro-environment and more physiologically relevant models. Several cell types are of particular interest in this context, namely those that are in some way protagonists in chronic diseases like diabetes, cardiovascular disease or cancer. Accordingly, the two fields of application for the developed prototypes presented in this chapter were on one hand undifferentiated pre-adipocytes and fully differentiated brown adipocytes, two types of adipose tissue cells which are thought to be the crucial players in obesity and in extension diabetes and only

recently have been confirmed to exist in humans. On the other hand vascular smooth muscle cells (VSMCs), which are studied extensively in relation with cardiovascular risk factors. Both cell types will be properly introduced later on in their respective sections.

The culture of (mammalian) cells inside microfluidic channels (µ-channels) can in itself be a delicate matter. First of all, physiological conditions (temperature $T = 37^{\circ}\mathrm{C}$, $pH = 5.5$, controlled gas atmosphere different from air) have to be established and maintained during the time of any experiment. In commonplace well-plate cultures this is usually achieved by placing the plates inside a so called 'incubator', which provides said controlled conditions. By gas diffusion through the culture medium, the cells are sustained with the right oxygen levels and pH. This necessity for gas diffusion is one of the reasons for the popularity of PDMS in LoC technology for cell cultures. The porous polymer matrix is gas permeable and thus permits cell culture in microfluidic channels using very similar procedures as applied in traditional well-plates. After injection of suspended cells into the µ-channel, LoC devices can be placed in the incubator without the need for continuous circulation of freshly diffused culture medium. The latter is however necessary if the construction material of the LoC is not permeable to gases, which is the case for the traditional silicon/glass architecture or thermoplastics like PMMA. Using PDMS, a periodic exchange of the culture medium inside the device is usually enough to achieve a proliferating two-dimensional cell culture.

As cells are injected into a µ-channel, they settle on the channel bottom according to The principal technical challenges arising in relation to the implementation of living cell monolayers as photonic component are summarized graphically in Fig-5.1 and should be viewed as three different blocks: The development of means for coupling of light into the 'living photonics', the design and implementation of the 'living photonics' themselves, and suitable means for light out-coupling at the receiving end. For the realisation of each block specific requirements are to be considered. The central block, the 'living photonics', consists of a bottom layer, correspond-

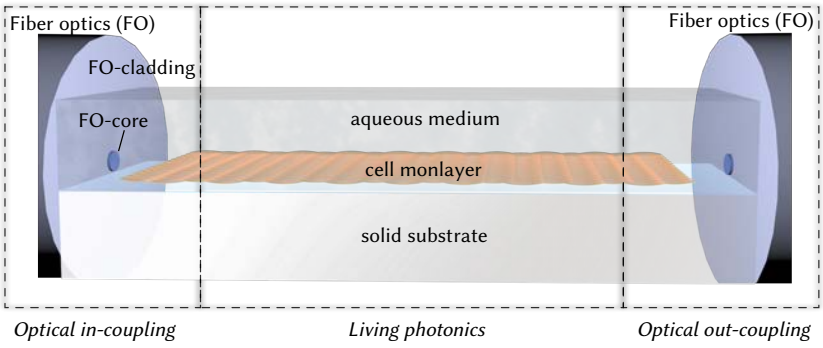

Figure 5.1: Graphical summary of the challenges faced in the implementation of living photonics.

ing to one of the construction materials of the PhLoC, the cell monolayer growing attached to said material and an aqueous culture medium covering the cells in a microfluidic channel.

According to what information can be found in the literature (see section 1.8 for details), the biological components to be implemented as photonic components can be expected to exhibit average refractive indexes $n_{\text{biomaterials}}$ in the range of $1.34 \lesssim n_{\text{biomaterials}} \lesssim 1.39$.

5.2 Simulations

5.2.1 Confinement and modal profiles in living waveguides

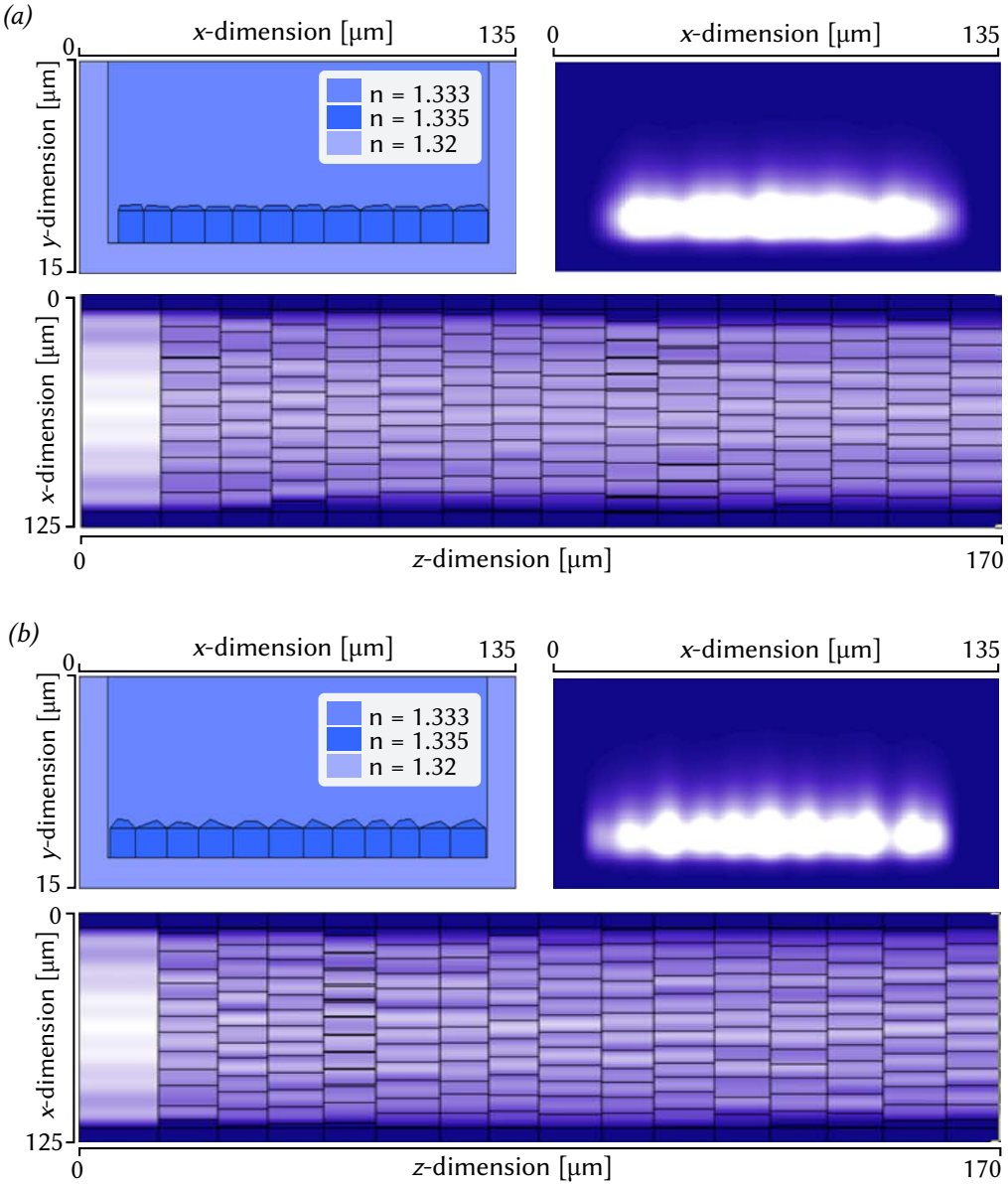

Figure 5.2: Modelling of light propagation through single layer living photonics. Rows correspond to cell-layers with height fluctuations of up to a) 0.2 µm and b) 0.4 µm. In the first column a representative example of the cross-sectional model geometry with RIs of n_{cells} = 1.335, $n_{support}$ = 1.32 and n_{medium} = 1.333 is shown for each case. The second column contains the calculated respective modal profiles, the third the light distribution along the cell-layer in top-view.

To get an idea of how light would propagate through a cell mono-layer given dimensionally adjusted light input, mode-matching numerical simulations have been carried out with the software-component FIMMPROP of Photon Design, a commercially available software designed for the calculation of mode-propagation in waveguides. The results are summarized in Figure 5.2. Two planar waveguides with different surface-roughness were implemented in order to model the influence of morphological changes in a cell mono-layer. Cells adhered to the bottom of the micro-fluidic channel are resembled by rectangles of certain constant height, which have trapezoids of random shape on top to simulate height fluctuations. The first rows in Figures 5.2 (a) and (b) respectively contains an example of the geometries of the cross-section of the monolayers as implemented. The different colors within the representation of the geometry on the left indicate the differences in refractive index (RI). The RI of the cells was assumed to be $n_{\text{cells}} = 1.335$, the RI of the culture medium as the upper cladding $n_{\text{medium}} = 1.333$. Bottom and side-walls of the fluidic channel were considered to have a RI of $n_{\text{support}} = 1.32$, which is well below the one of the cells. Both monolayers are between 2 and 2.6 µm in height. The one in Figure 5.2 (a) exhibits height fluctuations of up to 0.2 µm, the one in Figure 5.2 (b) up to 0.4 µm. The individual cells with widths between 8 µm and 12 µm were subsequently placed inside the channel, finally forming a row of connected cells.

In both cases, fifteen consecutive rows of varying appearance were then inserted in z-direction with random length between 8 and 12 µm, resulting in a model monolayer of around 150 µm length as it is shown in the top-view in the second row of Figures 5.2 (a) and (b), respectively. Light was coupled into the 'device' through a simple slab-waveguide without roughness (corresponding to the first slice in the top-view) of 2 µm height in order to model the coupling by an aligned integrated waveguide matching the dimensions of the monolayer. The second and third columns of Figure 5.2 contain a field plot of light of 532 nm wavelength traveling along the structure, calculated by FIMMPROP. The wavelength was chosen because it is in the middle of the visible spectrum. As expected, the results show rather strong confinement at the cell-support-interface, but considerable penetration into the liquid medium, as the RI difference is smaller there. Comparing a) and b) it is obvious that the modal profile is adjusting to the shape-variations introduced by the height-fluctuations. This results also in a difference in transmitted power. For smaller surface-roughness, around 45% of the initial power reaches the end-facet, 37% in the other case. These results suggest, that morphological changes will result in changes of the spectral response, as for different wavelengths different modes are available and transmittance will be affected differently. An important point to notice is that these results were obtained defining the input mode-profile as a rectangle matching the dimensions of the here 2 µm high base of the monolayer. For arbitrary light input, much more insertion loss is ex-

pected. In addition, a height of 2 µm will in reality only be the case at the sites of the cell-nuclei, whereas in between the height decreases to great extent according to how much cells stretch on the substrate. One of the crucial points apart from an appropriate refractive index environment will thus be efficient light insertion. And as a function of this insertion efficiency, it may become even more important to find ways to discard light that did not pass through the cells (Signal-to-Noise ratio).

5.2.2 Coupling means

Wide spectral range taper waveguide

The possibility of achieving efficient downscaling of the input power to the tentative dimensions of a cell monolayer was explored in the design and numerical optimisation of a wide spectral range tapered waveguide.

As convenient boundary conditions the initial width was fixed to 65 µm corresponding to a standard fiber-optics (FO) core-diameter. The final width was set to 2 µm, corresponding to a compromise between the resolution limit of standard PL and an optimistic estimate of average base height of a cell monolayer. The tapered waveguide has been designed and optimized for operation in the visible domain (400-750 nm). The 65 µm width at the input facet make this component suitable to act as a bridge between external input fiber-optics and on-chip integrated photonic elements.

Simulations and optimization have been carried out with the respective software-components FIMMPROP and KALLISTOS of Photon Design[1]. A taper-solver with a special algorithm for the near-adiabatic regime was applied, which dynamically splits the structure in successively smaller subsections and interpolates the overlap integrals through those sections. The final results for optimized shape and length (2730 µm) of the taper, given the constituting RIs of n = 1.58 (e. g. SU-8) and n = 1.32 (e.g. MY-123 A) respectively, are presented in Figure 5.3.

The spectral response is plotted as percentage of transmitted light staying in the fundamental mode, as a function of the in-coupled wavelength (between 400 and 750 nm). According to the calculations, more than 85 % of the in-coupled light stays in the fundamental mode throughout the spectrum, with a maximum of almost 98 % around 532 nm. The inset is a field-plot (at 532 nm), which visualizes how the light is confined in the tip of the taper and efficiently transmitted through a straight continuation of 65µm length and cross-sectional dimensions (2 µm in height, which here corresponds to the y-axis, and arbitrary width) similar to the expected Liphos'.

[1] Commercial Waveguide Mode Solver and Optimisation tool avaiable at Photon Design®

To complement these results, ray-tracing simulations of the same structure have been carried out with the commercial ray-tracing software TracePro. The results are shown in Fig. 5.4. Previous simulation results of over 90 % of the injected light reaching the tip could not be confirmed however implementing the same refractive index contrast.

What becomes much more apparent here than in the previous mode field simulations is the wide-angled optical output of the taper, which is in fact not surprising given the enormous mode scaling performed in the structure. The fabricated device, here replica moulded in PDMS and surrounded by air, shown on the bottom of Fig. 5.4 confirms the ray-tracing simulation of the taper output.

5.2.3 Optimised integrated micro-lenses

As an alternative for light coupling, a compound lens system was optimised for collimated output using the TracePro optimizer, defining parallel output beams at a distance of 5 mm as target

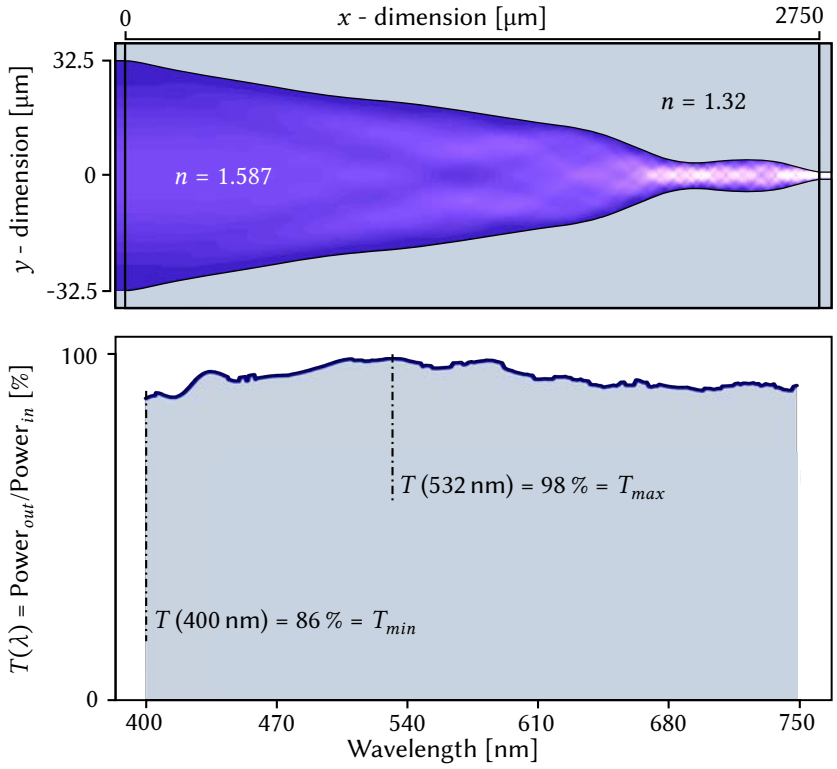

Figure 5.3: Spectral response of optimized taper shape calculated with Photon Design in the wavelength range from 400 nm to 750 nm. The inset displays the taper shape with width decreasing from 65 µm at $x = 0$ to 2 µm at $x = 2730$ µm. A field plot visualizes the light being confined to the tip of the taper.

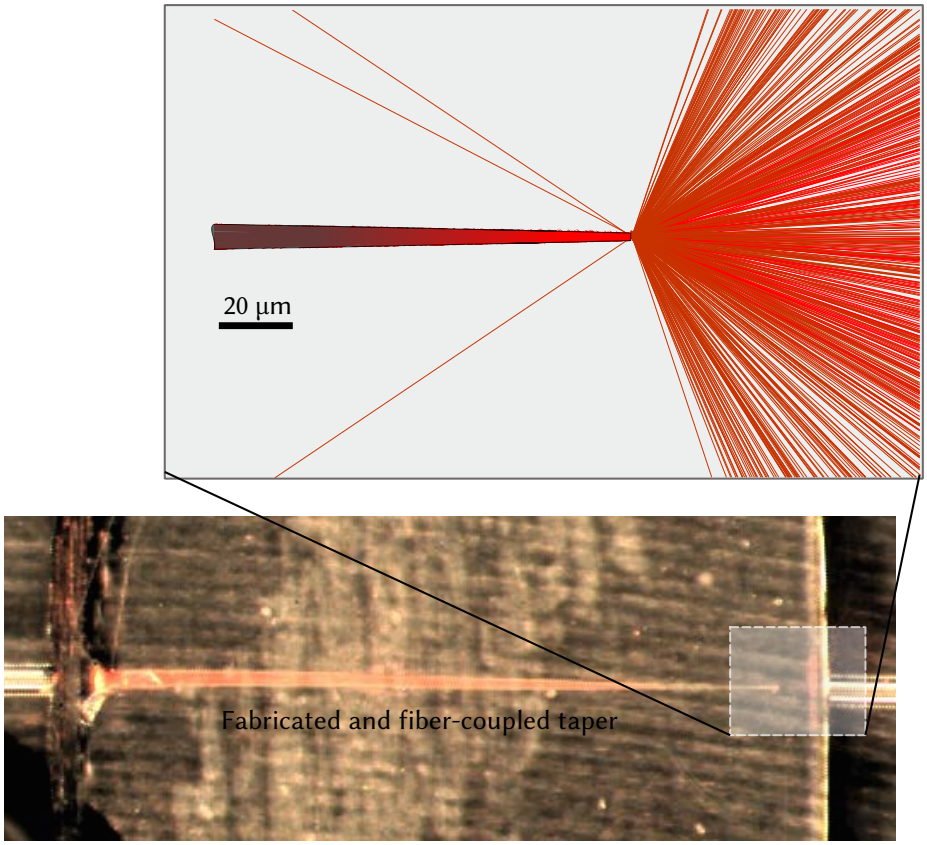

Figure 5.4: Ray tracing simulation of taper optimized using Photon Design in the wavelength range from 400 nm to 750 nm.

for the optimisation. The results for light propagation in plane of the optimised lens design are shown in experiment and simulation in Fig. 5.5. In the experiment, light propagation through a microfluidic chamber is observed indirectly by imaging the emission of a Fluorescein solution residing inside the chamber, which is excited by fiber-lens coupling using the newly designed and fabricated lens system and 105/125 µm fiber-optics. According to this experimental assessment, the experiment was consistent with the simulations. From the ray-tracing simulation additional information was gathered, displayed here as angular and spatial power distribution on the output-plane. Laying the origin of a polar coordinate system on the centre of the output-plane, the upper plot shows that all rays leave that plane at angles below 10° from the forward propagation direction. Further, the power distribution within these angles is spread wider in the up-down axis (z-axis) than in the lateral axis. This is also apparent in the mode-profile on the bottom, showing the power distribution per square meter to be confined within approximately $(0.2 \times 0.2)\text{mm}^2$ with the same tendency of incident power being focussed along the z-axis.

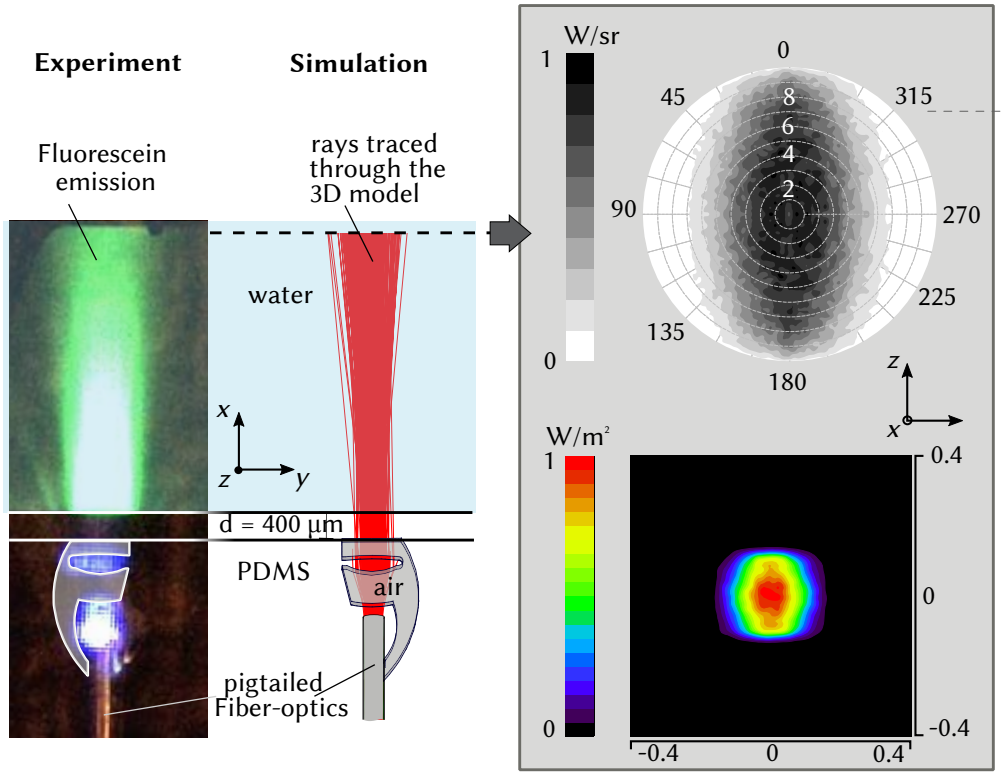

Figure 5.5: Experimental and simulation results of PDMS-air lens-system optimised using ray-tracing simulations in TracePro prior to fabrication. Left: Comparison of light propagation in the plane in experiment and simulation, Right: Ray-tracing analysis of angular and spatial power distributions after 5 mm optical path length in water.

5.3 Proposed strategies

5.3.1 'Vertical' configuration

The planar technologies used in soft lithography restrict geometries of optical elements to one plane and light will be focused in a plane perpendicular to said plane. Cell seeding however will be driven by gravity. So the design has to ensure that the monolayers will grow in plane with the focal plane of the integrated micro-optics. A micro-chip based on the proposed planar tapered waveguide and designed for fabrication using soft-lithography is proposed here. This chip-design in principle copes with all the challenges previously discussed and allows the implementation of living photonics in the from cell monolayers. However, a bio-compatible material with appropriate refractive index and properties suitable for structuring with soft lithography

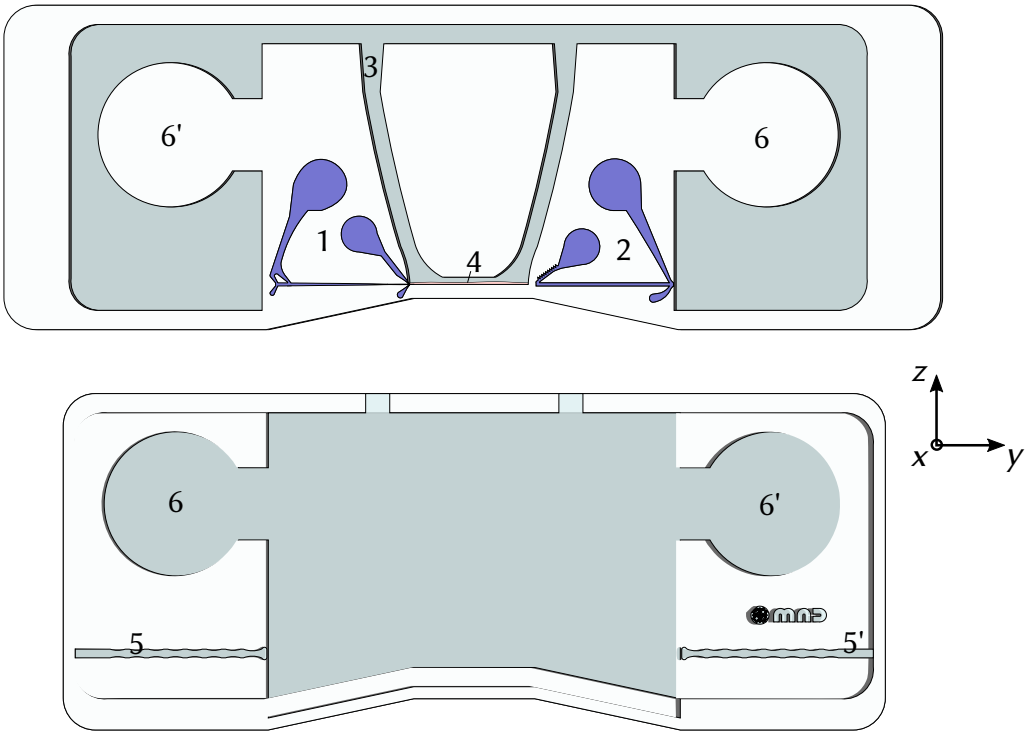

Figure 5.6: Parts of proposed 'vertical' photonic lab-on-chip configuration for the implementation of living photonics. (1) Negative of integrated tapered waveguide for in-coupling of light into the living photonics featuring two insertion sites for injection moulding of waveguide material. (2) Negative of straight integrated waveguide for collection of the optical output with identical insertion sites. (3) Fluidic channel. (4) Interrogation site: cells settle here and grow forming a mono-layer acting as living lightguide. (5, 5') Self-alignment channels for fiber-optics insertion. (6, 6') Auto-alignment structures for alignment of the two PhLOC-layers.

would be needed for its implementation. The model in Fig. 5.6 is a representation of the corresponding CAD-file, which would be used to fabricate the photo-masks involved in the master-fabrication. The back-plane of the chip (top of Fig. 5.6) contains a micro-fluidic channel (3) with a straight part of 1 mm length (4) between two integrated waveguides (1) and (2) contained as their negatives in the PhLoC-layer, as they need to be filled with a material with higher refractive index than the structural layer in concordance with the refractive index contrast established in the simulations. The rounded extensions at both ends of the integrated waveguides are insertion sites for injection moulding. The cells are supposed to grow on the bottom (yz-plane) of said straight part, forming the living lightguide. Light is in-coupled by a tapered waveguide (1) with a shape according to the simulation-results presented in Figure 5.3. Due to the fabrication method, the width of the taper (in x-direction) and the micro-fluidic channel are the same and a matched modal profile is achieved. For commonly used channel-widths (x-direction) of more than 125 µm, the tip of the tapered waveguide would need to have a very high aspect-ratio. The technological feasibility and performance of the taper with these restraints has to be verified prior to PhLoC fabrication. The straight integrated waveguide (2) at the opposite end of the interrogation site was added for light collection at the output of the living photonics. The front part of the chip (bottom of Fig. 5.6) contains self-alignment channels for insertion of optical fibers (5, 5') and seals the micro-fluidic channel. Rounded structures (6, 6') above the latter, of which the back-plane contains the negatives, play the double role of ensuring alignment of the two layers of the chip and increase the surface-area in order to improve bonding. For bonding, one of the layers would have to be flipped 180° around the z-axis with respect to the present representation so that structure 6 fits to 6 and 6' to 6', respectively.

5.3.2 'Planar' configuration

As alternative to the 'vertical' configuration, which has very specific technological requirements, it was also considered to start with more straight forward adjustments to the well established planar geometry of the PhLoC shown on the left-hand side of Fig. 5.7. As depicted in the scheme, this planar geometry comprises a microfluidic channel with a set of cylindrical lenses on either side and self-alignment structures to achieve controlled fiber-optics positioning. Such components are usually obtained in PDMS structured by standard cast-moulding as described in the introduction chapter and bonded to a suitable flat substrate. As mentioned above, this fabrication scheme has to be adjusted to satisfy the requirements established in Fig. 5.1 in terms of coupling and light guiding by the cell layer. Concretely, this means on one hand the incorporation of a base layer with refractive index lower than that of the cell monolayer. On the other

hand, alignment of auxiliary optical elements, which translates mainly to coincidence of the cell monolayer position in the out-of-plane z-axis with the centre of the fiber-optics, has to be ensured. As shown in the transversal views on the right of Fig. 5.7, an 'elevation' of the µ-channel bottom or alternatively embedding of the fiber-optics (FO) was proposed to achieve the latter. In addition, the optimised lens-system for collimated input (compare Fig. 5.5) was integrated in the design to improve the light coupling to the 'living photonics'.

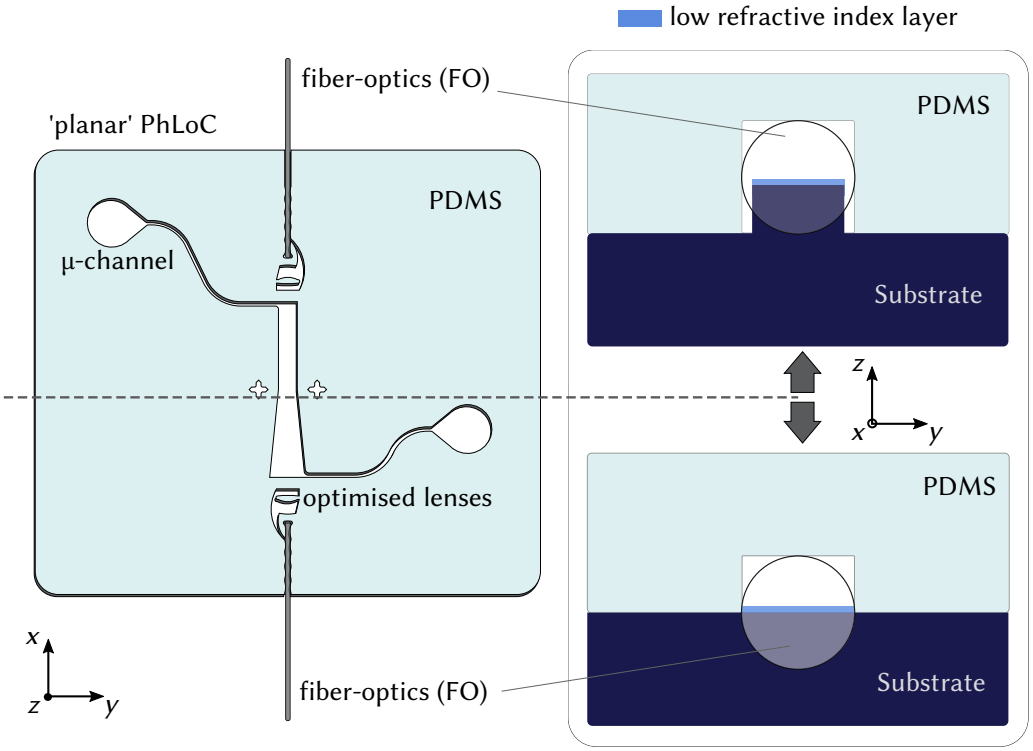

Figure 5.7: Left: Footprint of PhLoC in planar configuration. Right: Two approaches achieving 'z-alignment' of living photonics and fiber-optics.

5.4 Endothelial cell refractive index

Initial measurements of refractive index have been performed using index matching methods on the EA.hy926 cell line. By varying the density of sucrose in water, a corresponding well-defined change occurs in the refractive index of the medium n_{medium}. To perform the index matching by visual inspection via microscope, cells were washed, had their culture media removed and were re-suspended in various densities of sucrose and the outcome of the index matching experiment was recorded. The results obtained from successive cell suspension in sucrose solutions with increasing refractive index are summarised in Table 5.1. As shown in Fig. 5.8, the different

Table 5.1: EA.hy926 Cell Refractive Index Matching Results

Density g / cm3	% by Weight (w / v)	Refractive Index n	Outcome
1.0179	5	1.3403	RI too low
1.0299	8	1.3448	RI too low
1.044	11.5	1.3502	RI too low
1.0592	15	**1.3557**	Index match to **cell nucleus** (Fig. 5.8 (a))
1.0721	18	**1.3606**	Index match to **cell membrane**, nucleus distinguishable (Fig. 5.8 (b))
1.0854	21	1.3655	RI too high
1.0990	24	1.3706	RI too high

components of suspended cells can be 'matched' individually with the result that the phase contrast of the particular component in the microscope image is minimum. Fig. 5.8 (a) shows an example of n_{medium}. matching the refractive index of the cell nucleus, Fig. 5.8 (b) an example n_{medium} matching the cell membrane.

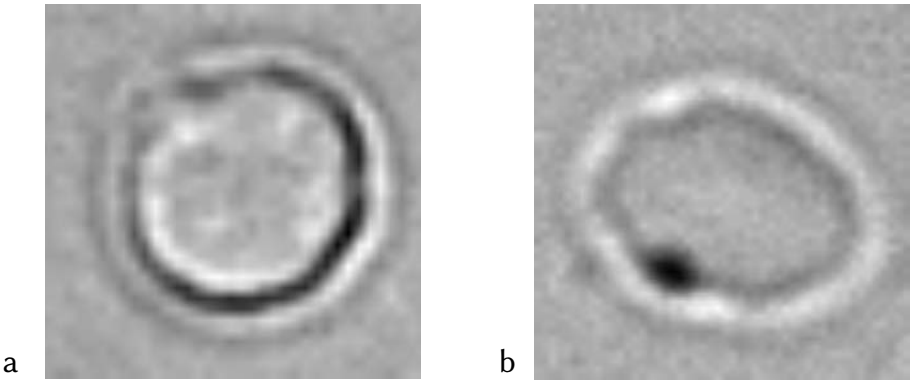

Figure 5.8: (a) Refractive index matching of EA.hy926 cell nuclei using Sucrose with refractive index $n_{nucleus}$ = 1.3557; (b) Refractive index matching of EA.hy926 cell membrane using Sucrose with refractive index $n_{membrane}$ = 1.3606. Here, cell nuclei become more distinguishable at this refractive index when compared to the cells in (a).

5.5 Low refractive index materials for PhLoCs

With the refractive index matching experiments shown above, it has been demonstrated that water or culture media respectively ($n_{\text{medium}} \approx 1.333$) provide a suitable boundary to achieve TIR inside cell-layers. However, the most biologically representative situations are often those where cells are attached to a substrate. In order to create such situations in the framework of a

PhLoC and promote light propagation in layers attached to the wall or bottom of a µ-channel, it would be highly desirable that said channel-wall or in the case of the planar configuration the substrate layer also be of a refractive index smaller than that of the cell-layer.
Unfortunately, materials like glass and many of the polymers commonly employed in MEMS and LoC do not cope with this requirement, as can be seen from table 5.2. Therefore, in the course of this thesis three different alternative materials were explored and characterized in terms of compatibility with the fabrication schemes at our disposal (compare section 1.5), refractive index and biocompatibility.

Table 5.2: Refractive indexes of common transparent structural materials in MEMS, LoC devices, and biological laboratories.

Material	Refractive index n (at 632.8 nm)
PDMS	1.4225 [*MicroChem Corp*, datasheet of Sylgard 184]
Fused silica	1.457 [Malitson, 1965]
PMMA	1.489 [Sultanova et al., 2009]
PC	1.58 [Sultanova et al., 2009]
SU-8	1.587 [*MicroChem Corp* datasheet of SU-8 2025 series]
PS	1.587 [Sultanova et al., 2009]

5.5.1 Fluorinated polymers

MY Polymers Ltd. provide a series of transparent polymers that are strongly fluorinated to reduce their refractive index to values as low as 1.31. At the time of writing this thesis, their product palette has been amplified considerably compared to what was available during our initial search for alternative materials. Then, the MY132A and MY133V2000 series seemed the most promising candidates for our purposes with refractive indexes of 1.32 and 1.33 respectively and the attribute 'bio-compatible' attached by the provider. Consequently, the following assessment will be restricted to these two compounds, which were purchased at 16.67 €/g. [2]
The UV-curable polymers were distributed as adhesives for bio-applications and the technical data-sheet claimed they be non-cytotoxic. Micro-structuring however had not been done before. For improved adhesion on glass or plastic, the manufacturer provided the primers *Primer G* and *Primer P* respectively.

[2]For comparison, the typical PDMS kit - Sylgard 184 (Dow Corning Corp.)- is available at around 30\$kg^{-1}.

Processing

From the point of view of micro-fabrication, processing of the materials was at first glance compatible with the standard protocols used in our department (compare sections 1.5.1 and 1.5.1). As initially viscous liquids and flexible after curing, the polymers were well suited for cast moulding. One critical aspect for successful curing was however the need for an inert atmosphere, which implied some complication to the process. The optimisation of the curing process was unfortunately not as straight-forward as expected. Different strategies were tested with little success in most cases.To avoid the exposure to air during the curing, nitrogen-atmosphere and curing under water were tested initially. In general, the manufacturer recommends an exposure dose of at least 4 J/cm^2 EOC [2013]. Curing under water however, has been found to require at least 6 J/cm^2 and still a superficial layer of uncured pre-polymer remained. For curing in PDMS replica it was crucial to apply an adhesion primer (also purchased from MY Polymers) prior to injection of the fluorinated pre-polymers, which probably stopped the contact with diffused oxygen through the porous PDMS matrix. Even then, the success rate was rather low. The details of the optimisation process are listed in the appendix, section C.2. The most reproducible solutions were to use a two level master mould, which implies two photomasks and therefore an increase in process costs, and cover the uncured polymer with a flexible film to impede contact with oxygen as depicted in Fig. 5.9a. Another option was the use of a polymer replica for injection moulding as detailed in as depicted in Fig. 5.9b.

In the end, the fabrication of micro-structures of both MY-132A and MY-133-V200 has been successfully fabricated on glass- and PDMS-substrates with and without primers, using PDMS as well as SU-8 master moulds. Figure 5.10 is a microscope-image of a pillar-structure of MY-132A, which was created by injection moulding on a PDMS-substrate using a PDMS-mould fabricated

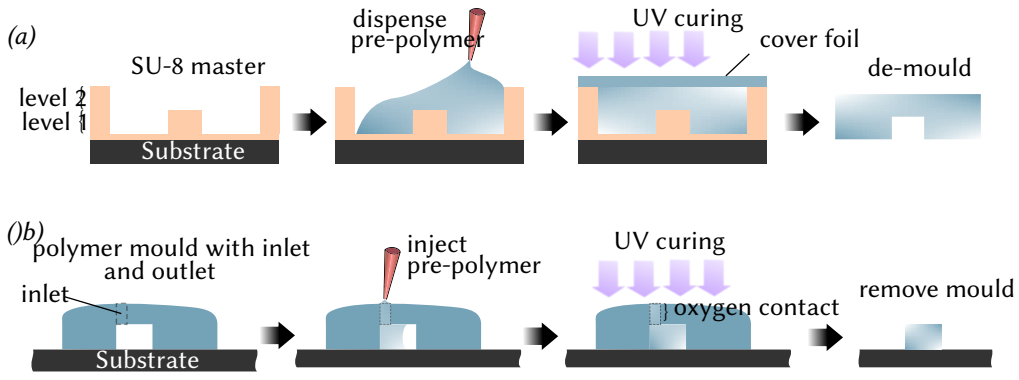

Figure 5.9: Microfabrication strategies for MY-polymers. (a) Mould casting using two-level SU-8 master mould and PET cover foil to avoid air contact of the pre-polymer during exposure. (b) Injection moulding using a primed polymer replica of an SU-8 master mould and a primed substrate.

with soft lithography. The substrate was previously coated (using a paint brush) with Primer G. The surface-roughness visible in Figure 5.10 is created by said coating, but could be essentially reduced by the use of an air-brush. The central pillar is 650 µm, the arms leading to the rounded injection sites 160 µm wide and the whole structure is 125 µm high. The mechanically obtained height-profile of the structure in Figure 5.10 confirms vertical walls and thus excellent performance of the molding-procedure. The results correspond to measurements of the central piece of the structure at three different positions, indicated by the three lines across the pillar in the photograph detail. Given these properties, the polymers appeared to be a real alternative for PDMS, allowing for fabrication processes like mould casting and injection moulding, but offering the desired n.

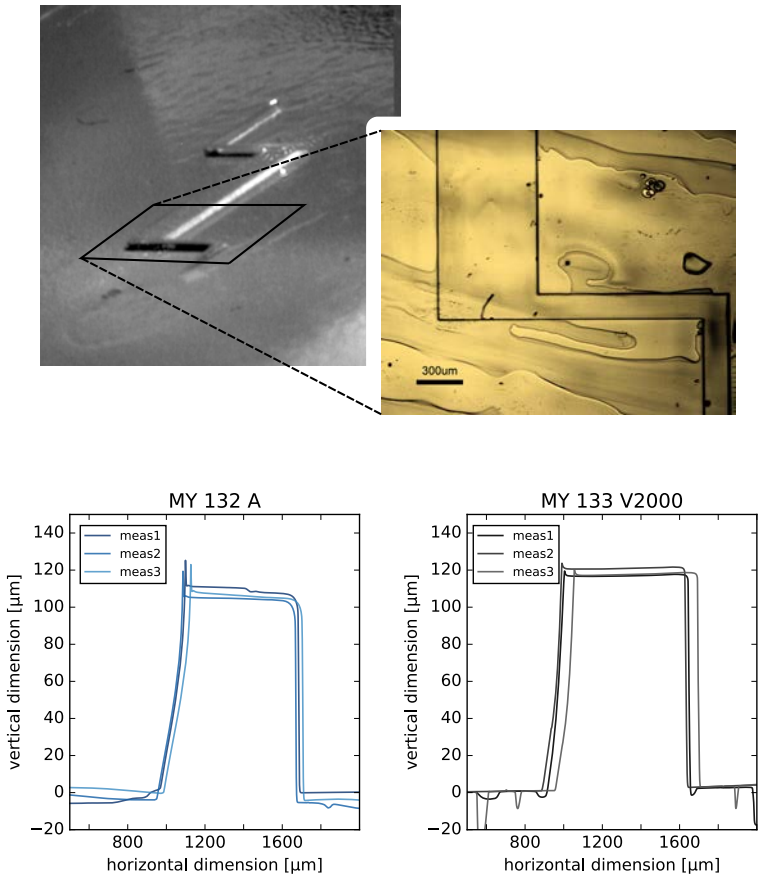

Figure 5.10: Validation of MY-polymer compatibility with soft-lithography. (top-left) Micropillar for vertical alignment fabricated in MY 132 A using a PDMS mould, (top-right) microscope image of the same micropillar, (bottom) height profiles of MY-polymer micropillars measured with mechanical profiler (Tercor alpha step 200).

Optical characterisation

Prism-coupling.

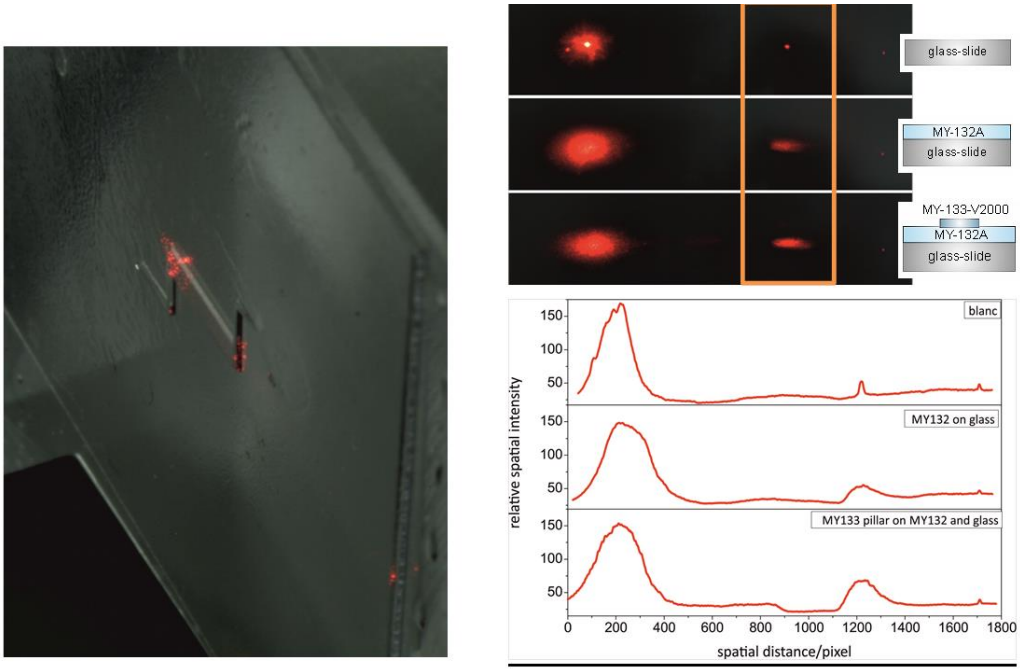

FIGURE 5.11: Prism-coupling of a laser (633 nm) to the model waveguide (MY-133 V2000 pillar on MY 132A coated glass-slide). The photograph on the left shows how light is coupled to the waveguide. The right shows the relative spatial intensity output profiles for the three cases 'blanc' (only glass-slide), 'MY-132A on glass' and model-waveguide from top to bottom respectively.

Figure 5.11 shows the results of the prism coupling. As can be seen in the photograph at the left, light is coupled in the waveguide core, which confirms that even with a small refractive index difference between the core and the cladding, light confinement can be experimentally observed. Here, from a photonic point of view, it is confirmed how a cell culture would behave as the bio-waveguide core using a material with lower n as cladding, and that light may be coupled to such a bio-waveguide.

However, this coupling method reveals certain problems. To get an idea of the intensity effectively confined by the waveguide, the light intensity in the direction of the prism edge (~1200 pixels spatial distance and highlighted with a frame in the corresponding photographs) was compared with the reference models schematically shown in the insets. As can be seen, a small peak in this direction is already present for an uncoated glass-slide, probably due to the non-perfectly matching refractive indexes of immersion oil and glass-slide, leading to light guidance along the interface. For unclear reasons, this effect is even increased after adding a layer of MY-132 A. Finally, adding the actual waveguide, intensity increases again in the direc-

tion of the output. Light confinement in the structure is confirmed both by the scattered light at the end-facet of the pillar-structure and the increase of intensity at the output, but an evaluation of the coupling efficiency is quite difficult due to the multiple interfaces involved in this configuration. Apart from that, another obvious disadvantage of this coupling approach is that due to the RI contrasts, depending on the angle, a major amount of light is either lost by total internal reflection at the prism/glass-slide interface and does not even reach the sample (like the case in the results at the right hand side of Figure 5.11, see peaks around 200 pixels spatial distance), or enters the waveguide with an incidence angle too small to allow internal reflection and thus confinement inside the structure. As a result, the intensity of the peaks around 1700 pixels spatial distance would be increased instead. It is worth noting that the experiment was performed in air, which means that the upper cladding of the waveguide has not the RI of 1.333 of the culture medium, but a RI of n = 1, allowing light of smaller angles of incidence to be totally internally reflected (guided) inside the structure. For n=1.33 the required incidence angle at the cell medium interface is > 82° and cannot be reached in this configuration. Additionally, this coupling angle is wavelength-dependent, which means that the coupling of a broadband light source would require precise angle adjustment and correlated wavelength scanning. Thus, in addition to the complication this means for the experimental setup, a lot of time-resolution would be lost, inducing an acquisition delay while obtaining the data for the PIN.

Direct fiber-coupling.

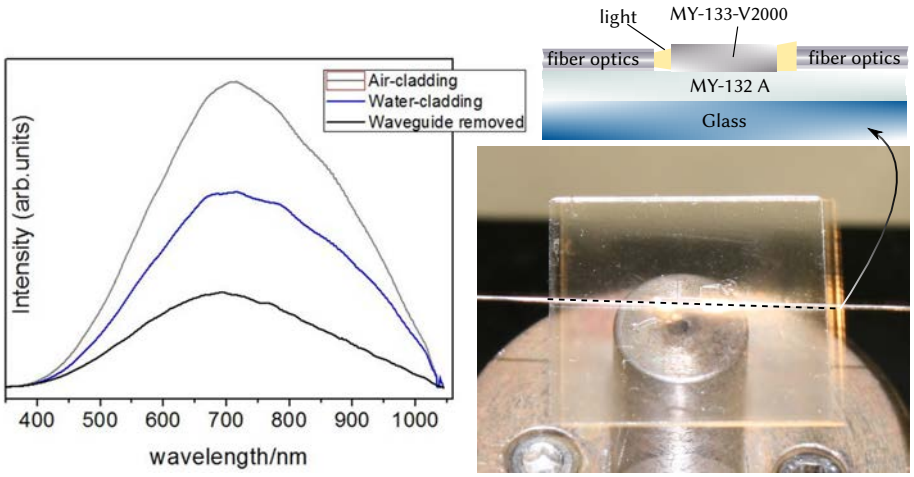

FIGURE 5.12: Validation of MY-polymer refractive indexes. (bottom-right) Photograph of micropillar fabricated in MY-133 V2000 on a glass slide coated with MY-132 A; (top-right) schematic of the longitudinal cut indicated in the photograph; (left) Light transmission with (i) air surrounding the micro-structure, (ii) a drop of water covering the surface including both tips of the fiber-optics, (iii) sample removed from between the fiber optics.

To tackle the prism coupling drawbacks, the initial configuration, namely direct fiber coupling, was also implemented. Optical fibers were placed at the two ends of the central, straight part of the pillar structure, as was shown in the photograph in Fig. 5.11. Alignment of the fibers at the front and end cleavage was achieved with two piezo-stages. The spectral response was obtained by connecting a halogen lamp and measuring transmission with the spectrometer. The pillar structure exhibits the typical appearance of a waveguide with light only visible at the front and end facets due to scattering. The intensity of these two spots, especially at the right (output) facet, suggests a large insertion loss, which is due to the difference in size and shape. The fibers and pillar have the same height, but the pillar has more than four times their width, so in particular, coupling from the pillar to the output fiber causes a large loss of intensity.
Transmission was measured with air and distilled water as upper cladding of the model waveguide and in the case of its removal from between the fiber optics. The n of air is 1 and the n of distilled water is about 1.33 in the visible range. As the latter is matching the n of the waveguide material (MY-133-V200, n = 1.333), confinement inside the structure should be high for the air cladding. Hence, one expects the intensity reaching the second fiber to be highest for the waveguide with air as upper cladding in between and to drop subsequently in the case of water covering the pillar structure and removal of the waveguide. In the case of the water cladding, the transmitted intensity depends on the degree of confinement. The results are also plotted in Fig. 5.11). As expected, for the waveguide with air cladding, the intensity reaching the output

fiber was the highest. Removing the waveguide, the intensity dropped drastically. To realize the water cladding, which is closer to the real case, a droplet of distilled water was placed on top of the pillar structure without touching the fiber optics. Intensity dropped to a level just around the middle of that in the two other cases, which means decrease of the number of guided modes, or, in other words, a decrease on the light power confinement. Still, a reasonable and measurable amount of light reaches the readout.
Of course the dimensions of this experiment are not comparable with the real application. Still, confinement has been demonstrated with a n-matching model, and the MY-132 A proved suitable as support material. Comparing the coupling methods, it has become clear that direct coupling to the waveguide with dimensionally matching optical elements is much more predictable than prism coupling. Additionally, obtaining a spectral response (PIN) with prism coupling will involve a quite elaborated setup and induce time delay to obtain the PIN.

Biocompatibility

Viability of vascular smooth muscle cells (VSMC) from rat aorta exposed to MY-132A and MY-133 V2000 samples was evaluated using the colorimetric MTT (3-(4,5-dimethyl-thiazol-2-yl)-2,5-diphenyl-tetrazolium bromide) assay. Viable cells transform MTT salt into formazan dyes so that a quantitative measure of cell viability can be obtained comparing the optical density after incubating in contact with MY-polymer with the initial one. The results on the left hand side of Fig. 5.13 are based on a misinterpretation of the weights of the polymer pieces. Samples of pieces of MY-132A (stored between glass-slides at room temperature in contact with air for three month) of similar size/surface area, but put together in groups of 2, 3 .., 6 pieces, had been shipped for testing. The total weight of each group was measured beforehand and the samples were sent in triplicates for the same number of polymer-pieces. However, for the assay only one piece was used as representative of each group. Considering that the total weight of one group was not divided equally on it's constituents, a quantitative tendency like concluded in the graph is not representative. Still, it was clear that in some cases the single piece of MY-132A introduced into a well-plate produced measurable changes in the viability of the tested VSMCs. To conduct a second and more conclusive test, freshly prepared sheets of MY-132A and MY-133 V2000 were cut in pieces with subsequently increasing surface area (details in Table 5.3) up to an area corresponding to 56% of the area of one well of a 96x-wellplate. The results are summarized on the right hand side of Fig 5.13.

Table 5.3: Surface areas of tested polymer-pieces.

Dimensions	Area	% of well-area
(2x1.5x0.17) mm	7.21 mm^2	22.4
(2x2x0.17) mm	9.36 mm^2	29.11
(2x2.5x0.17) mm	11.53 mm^2	35.9
(2x3x0.17) mm	13.68 mm^2	42.55
(2x4x0.17) mm	18.04 mm^2	56.1

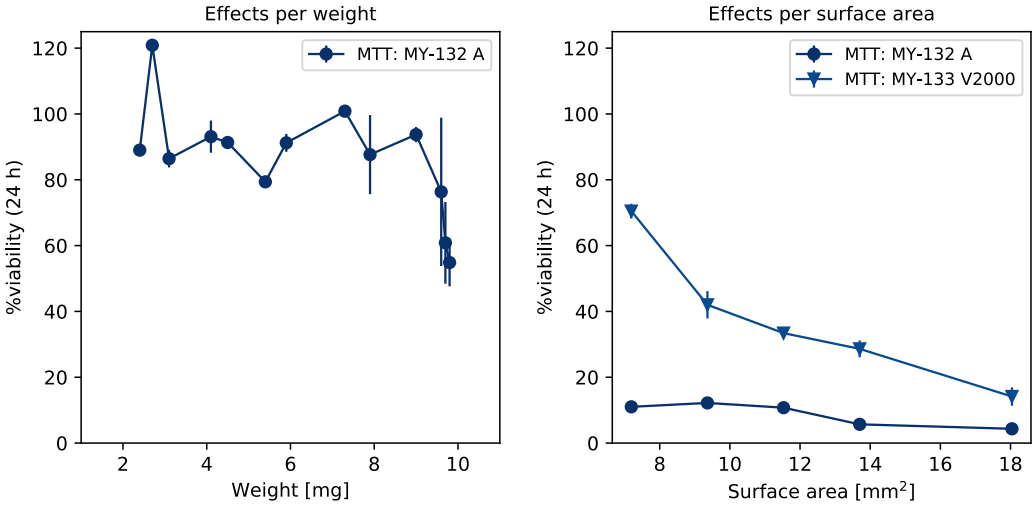

Figure 5.13: Validation of MY-polymer biocompatibility using an MTT (3-(4,5-dimethylthiazol-2-yl)-2,5-diphenyltetrazolium bromide) assay on vascular smooth muscle cells (VSMCs)

Considering only this second test, both untreated MY-polymers and particularly MY-132A are cytotoxic. For MY-132A, cell-viability doesn't exceed the 10 %, even for the smallest amount of polymer added. The fact however, that in the first test most of the samples showed a viability between 80 % and 90 %, suggests the possibility of cleaning to remove toxic substances like residual (un-crosslinked) monomeres or rests curing-agent. A strategy to remove residual monomeres would be washing with acetone, as the un-crosslinked resist dissolves in esters and ketones. Nevertheless, as a result of these tests the search for alternative materials or configurations was made priority.

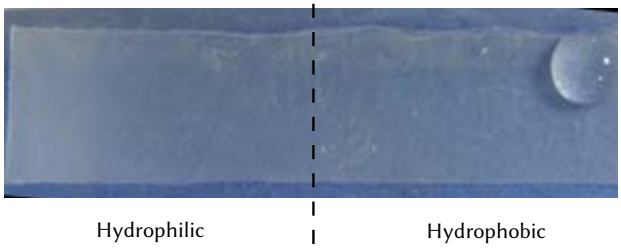

Figure 5.14: Demonstration of bulk functionalisation rendering the initially hydrophilic (left-hand side)v bacterial cellulose sample locally hydrophobic (right-hand side). Photograph reprinted with courtesy of the Group of Anna Roig.

5.5.2 Bacterial cellulose

BC was identified as alternative material with possibly low refractive index caused by a high degree of porosity. Through contact with Anna Roig from ICMAB we were pointed towards bacterial cellulose as another alternative material. Due to the high degree of porosity that can achieved (60% to 90%), the average refractive index was expected to be fairly similar to that of water, once wet. They kindly provided us with samples in form of thin sheets, whose characterisation is presented following. Preliminary studies with HELA cells showed proliferation of cells exclusively on the surface of the material, suggesting that the pores are small compared to the cell-size. Being a composite material, it's refractive index will be determined by the refractive indexes of the constituent materials. These are $n = 1.54 - 1.62$ for the BC-fibers and the refractive index of the material filling the pores. Considering air as the latter, the effective refractive index can be reduced significantly increasing the degree of porosity. The lower limit however will always be the refractive index of the material inside the pores. In the scope of this project this will be culture medium, which as aqueous solution has a refractive index of around $n = 1.333$. To that end it is worth to mention that the present BC can be rendered hydrophobic (see Figure 5.14) such that no water enters the pores and providing the possibility to approach $n = 1$ as much as porosity allows.

5.5.2.1 Processing

The material can be covalently bonded to PDMS though, allowing in principle the integration with established fabrication methods. The thin sheets as raw material however restricted the processing options to cutting tools such as scissors, cutting plotter or even laser cutting. With respect to the integration of the resulting material samples into a PhLoC architecture, the procedure illustrated in Fig. 5.15 conveys the general idea. The cutting process with the scalpel blade

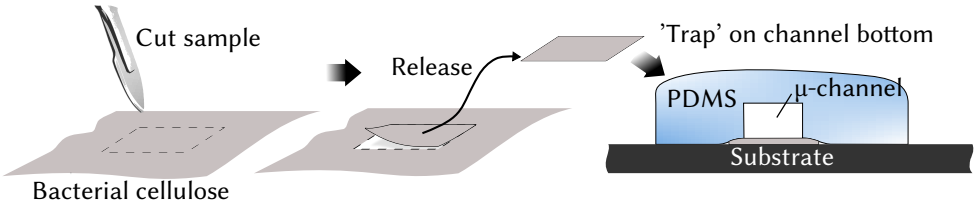

Figure 5.15: Manual fabrication process for the integration of bacterial cellulose (BC) layers into the PhLoC architecture. After cutting the samples to size, the surfaces of substrate, mould and BC surfaces were O_2-plasma activated and aligned to each other as indicated for bonding.

is representative for any available cutting method. After cutting the samples to size, the surfaces of substrate, mould and BC surfaces were O_2-plasma activated and aligned to each other as indicated for bonding. The plasma activation resulted in the aforementioned covalent bonds with the PDMS moulds as well as the glass substrate.

5.5.2.2 Material properties

Refractive index. The refractive index of the 90 % porous BC in the wet state was determined by "immersion refractometry", also called "index matching" on occasion. Light transmission through the BC was measured as a function of refractive index of the liquid medium in a BC-chip of type A (see Figure 5.15). To that end, the channel has been subsequently been filled with aqueous sucrose solutions of increasing concentration. Sucrose solutions are commercial refractive index standard, as the change in their RI is very well known as a function of concentration[3]. If the RI of the BC is different from that of the immersion medium, light passing the channel is scattered, resulting in a reduction of transmission for the whole spectrum. So maximal transmission is expected for matched RIs. The results shown in Figure **??** originate from repeated measurements and state an effective RI of around 1.339 for the wet state.

[3]Refractive index values of aqueous sucrose solutions are available at the time of writing in fully tabulated form at the Cell Biology Laboratory Manual of Dr. William H. Heidcamp, Biology Department, Gustavus Adolphus College, St. Peter, MN 56082 – cellab@gac.edu

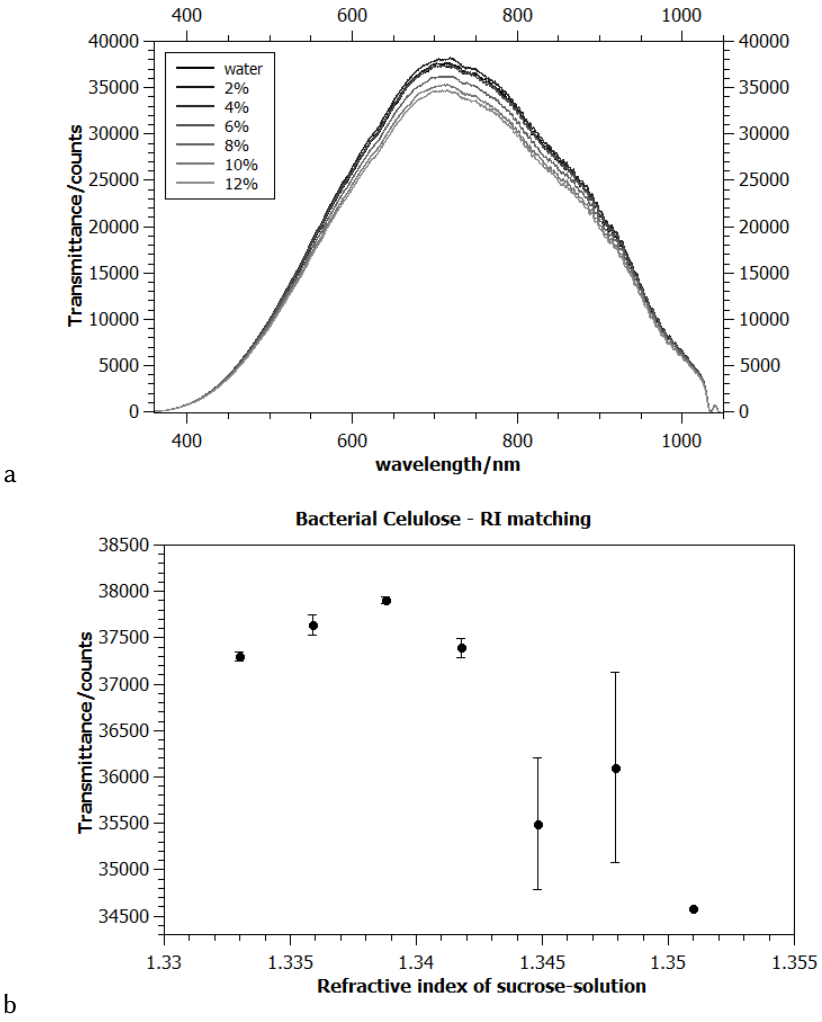

Figure 5.16: Determiniation of refractive index via index matching using sucrose solutions with well-defined optical properties. (Left) Series of transmittance spectra of BC-chip filled with aqueous sucrose solutions of different concentrations. (Right) Transmittance values at 700 nm as a function of n of immersion medium.

5.5.2.3 Biocompatibility

Due to the biological synthesis of the material, which is performed by bacteria, biocompatibility was the least problematic point in this case. As shown in Fig. **??**, different cell lines successfully formed confluent layers on the samples.

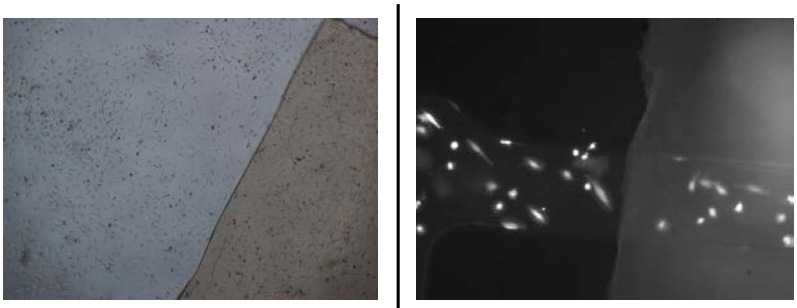

Macrophages (after 36 h) | Calcein stained HUVECs

Figure 5.17: Microscope images of different cell lines growing on bacterial cellulose (BC). Left: Macrophages growing in well-plate partly covered with BC; Right: HUVECs in µ-channel equipped with BC.

Swelling characteristics

For an initial assessment of the BC layer as constituent material in a PhLoC, one sample bonded in the described way was studied in terms of surface morphology. Figure 5.18 shows the results of confocal microscopy imaging on a dry BC sample plasma-bonded to a glass slide and fixed on both sides by two PDMS slides with 3 mm distance. The results show that the initial samples are already quite heterogeneous in thickness, with height fluctuations around 10µm with a total film thickness varying between 10 µm and 20 µm .

Swelling characteristics of the BC inside a microfluidic channel as depicted in Fig. 5.15 have been evaluated by confocal microscopy and image processing. Fig. 5.19 (top) shows images taken from the cross-section of a PDMS-microchannel with BC trapped on the channel-bottom and bonded to a glass-slide as substrate.

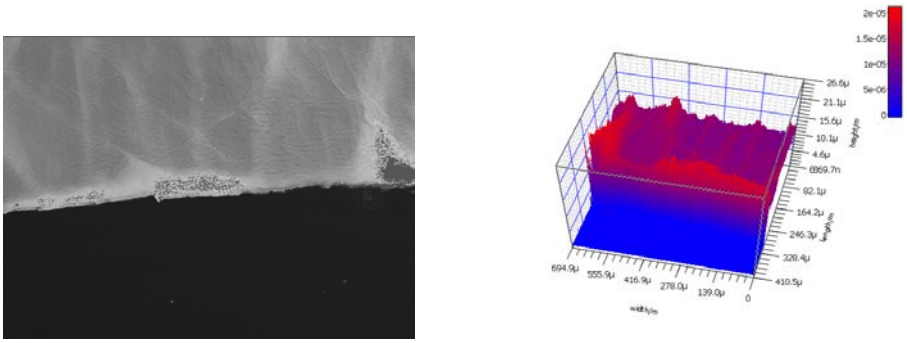

Figure 5.18: (Left hand side)Confocal microscope image of BC fixed on glass between two PDMS-pieces. (Right hand side) 3D-representation of the microscopy data, revealing thicknesses of 10-20 µm .

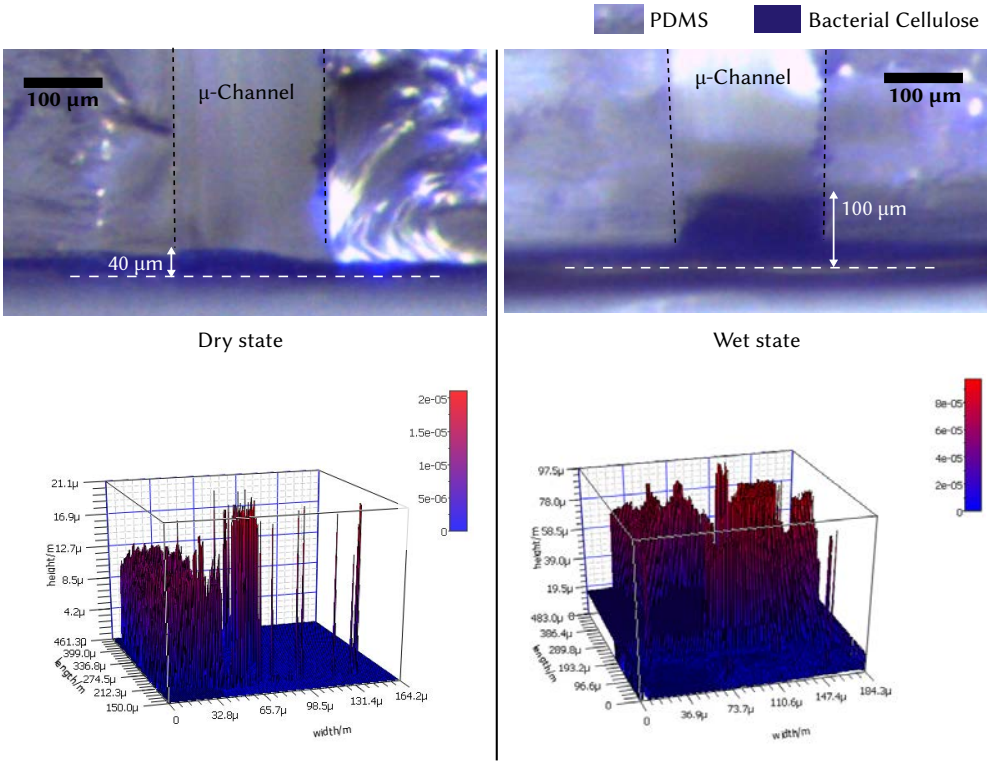

Figure 5.19: Swelling characteristics. Cross-section of microchannel with Crystal violet dyed BC on the channel bottom. (Left) Dry BC (after removal of the Crystal violet solution) shows a thickness of 20-40 µm *, meaning it does not fully recover the initial values of 10-20* µm *. (Right) Wet BC (channel filled with water) reaches a thickness of around 100* µm *.*

Measurements with ImageJ[4] reveal thicknesses of 20-30 µm in the dry state (after one wetting cycle) and around 100 µm in the wet state. Confocal microscopy in a chip with the same configuration, but without dying, gives similar results. Fig. 5.19 (bottom) shows the 3D-representations of the image-stack obtained with the confocal microscope. The piece of BC incorporated in this chip showed much more heterogeneous thicknesses then the one evaluated visually. Only a small fraction of the area under observation presented a thickness within the range of 40 µm used for the scan (the range was adjusted taking into account the previous results) in the dry state. The same applies for the wet state, where the scanning range was adjusted to 60-120 µm thickness.

The observed surface heterogeneities and liquid induced thickness fluctuations were very large compared to the estimated height of a cell monolayer and thus may hinder considerably the establishment of proper z-alignment of the latter and fiber-optics during optical measurements.

[4] Abramoff, M.D., Magalhaes, P.J., Ram, S.J. "Image Processing with ImageJ". Biophotonics International, volume 11, issue 7, pp. 36-42, 2004.

In combination with the rather cumbersome manual PhLoC assembly, further material systems were explored for integration into the proposed PhLoC platform.

5.5.3 Porous silica xerogel films - (TEOS)

The last solution explored in this work was a highly porous material obtained using a micelle assisted sol-gel method based on the work of Karasiński [2006], Karasiński et al. [2011]. In said prior works, mainly dip-coating was used to deposit thin layers of up to 650 nm thickness with refractive indexes below $n = 1.35$ for the dry films.

Cleanroom processing.

In order to adapt the method to the local cleanroom facilities, a spin-coating process was optimised for silicon and Pyrex wafers in order to achieve uniform layers on wafer-level. The resulting procedure was as follows: Tetraethyl ortosilicane $Si(OC_2H_5)_4$ (TEOS) was mixed with the non-polar surfactant Triton X-100 according to the protocol defined in the Appendix, chapter **??**. The resulting gel was spin-coated at 400 rpm on a silicon wafer with a 400 nm thick layer on the surface. Subsequently, the coated wafer was heated in an oven to 450°C with a ramp of 2°C /min, kept at this temperature for 30 min and cooled down to room temperature again with a ramp of 2°C /min to avoid thermal stress. Heating like this to 450°C resulted in the annealing of the micellar inclusions while avoiding a collapse of the porous structure and thus creating a porous *sol-gel* matrix was obtained.

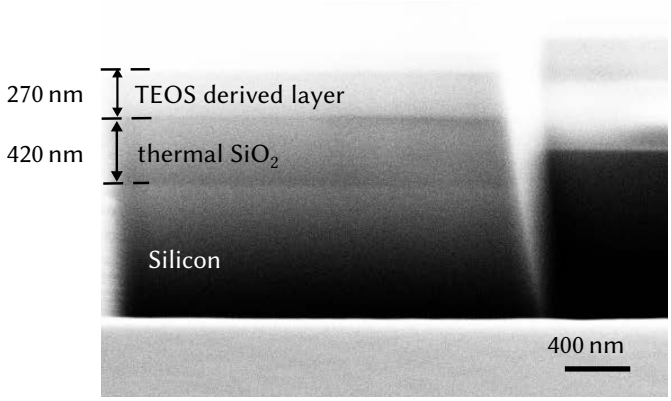

Figure 5.20: FIB-image of silicon wafer with a thin layer of thermal oxide and a thinfilm of TEOS deposited on top. The different layers are indicated by dashed lines and the film-thickness measures obtained with the FIB are 300 nm for TEOS and 400 nm for the thermal oxide.

Table 5.4: Ellipsometry measurements on TEOS-derived thinlayers.

Measurement	layer thickness [nm]	refractive index n_{TEOS}
dry 1	289	1.268
dry 2	299	1.271
dry average	294 ± 5	1.27 ± 0.002
wet 1	277	1.368
wet 2	296	1.331
wet3	298	1.32
wet4	306	1.314
wet average	294 ± 17	1.333 ± 0.035

In Figure 5.20 a FIB-image is shown, indicating the measures of the layered structure. Even at this high magnification, the pores are not resolved, which means that pore-size was in average well below 100 nm or collapsed on the cutting edge created by the FIB. The obtained thinfilms had a thickness of approximately 300 nm (estimated using ellipsometry and confirmed by FIB-imaging) and exhibited a RI of $n = 1.270 \pm 0.002$ (measured using ellipsometry on the dry film at 635 nm, compare Table. 5.4). Unfortunately, corresponding refractive index measurements in the wet state were subject to much more uncertainty in the measurement due to the lack of suitable equipment. In average, a refractive index $n_{TEOS-wet} = 1.333 \pm 0.035$ was obtained by dispensing a droplet of water on the surface of the layer and measuring next to the border of said droplet, where the TEOS-derived layer was visibly wet almost instantly upon dispensing the droplet, probably due to capillarity and an apparently hydrophilic surface (we observed a very large contact angle).

Biocompatibility

Bio-compatibility of TEOS-films was validated by culturing cells inside the channels of a PhLoC in planar configuration comprising a micro-structured TEOS film on the channel bottom (Fig. 5.21), the fabrication of which will be detailed as part of the following sections.

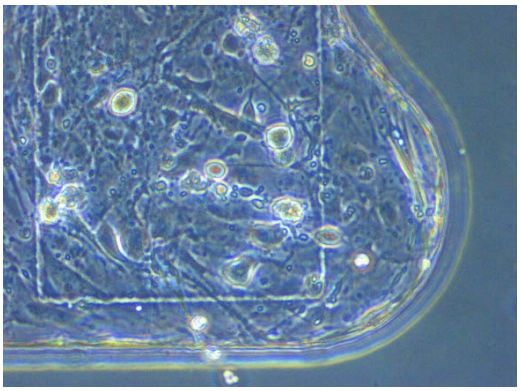

Figure 5.21: Section of μ-channel in TEOS coated chip, cells adhering on the underlying TEOS-layer inside the micro-channel.

5.5.4 Conclusions

Three different materials have been investigated for their incorporation into PhLoC-configurations to achieve zones therein with suitable refractive index to allow the implementation of living cell monolayers as photonic elements. Low refractive index fluorinated polymers as the suitable candidate for the realisation of the proposed 'vertical' configuration were compatible with traditional soft-lithography techniques but had to be discarded as they interfered negatively with cell proliferation, being highly hydrophobic and lowering cell viability considerably after 24 h of culture. Bacterial cellulose as a material with suitably low refractive index in the visible range (yet slightly greater than that of water), proofed an interesting material for optical applications with cells due to its bio-compability, but was discarded for the application at hand due to uncontrolled height fluctuations which appeared to be enhanced upon wetting. TEOS-based porous silica films were the altogether most robust solution from a technological point-of-view and featured furthermore the lowest refractive index in the dry state and with $n_{TEOS-wet} = 1.333 \pm 0.035$ a suitably low refractive index in the wet state to establish TIR conditions in an attached cell monolayer.

5.6 PhLoCs for in-vitro monitoring of inflammatory process in various cell types

5.6.1 Design and Fabrication

5.6.1.1 Overview of technological advances.

Fig. 5.22 summarises the evolvement and technological choices made in the course of developing a low refractive PhLoCs suitable for the implementation of monolayer living photonics.

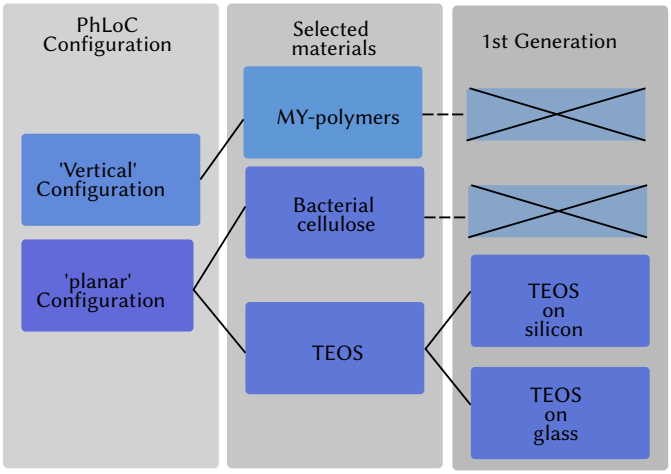

Figure 5.22: Evolutionary tree for low refractive index PhLoCs as developed in this chapter.

5.6.1.2 TEOS on silicon

As a consequence of the conclusions drawn from the extensive characterisation of low-refractie index materials detailed previously, in a first approach towards monolayer living photonics, we used the initial TEOS on silicon technology presented in the previous section to create a PhLoC according to the 'planar' scheme shown in Fig. 5.7. To achieve the cross-section displayed on top of the right side, and thus elevating the living photonics to the center of the fiber-optics, TEOS was processed by spin-coating on a silicon wafer as described previously. After that, two steps of photolithography and subsequent reactive ion etching (RIE and DRIE respectively, compare sections 1.5.1 and 1.5.1) were applied to remove 62.6 µm of material from the surface of the wafer, leaving untouched only the masked regions corresponding to the bottom of the µ-channel as shown in Fig. 5.23. The polymeric layer comprising the fluidic channel and TIR-based optical elements were fabricated by replica moulding in PDMS and bonded to the patterned

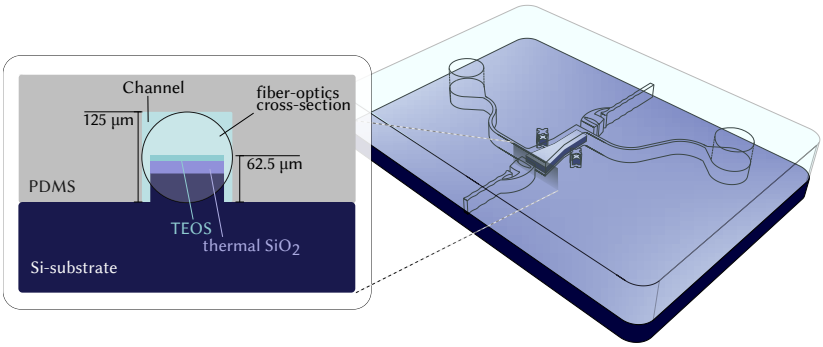

FIGURE 5.23: Initial PhLoC design scheme comprising TEOS coated micropillar for vertical alignment.

silicon/TEOS substrates by applying O_2-plasma to both layers during 18 seconds. The resulting PhLoC is shown in Fig. 5.24 (a). The opaque silicon substrate turned out to be a major obstacle for the visual control of the cell cultures, as three of four collaborating bio-medical laboratories are equipped with only inverted microscopes. The developed technology therefore had to be transferred to transparent substrate. This step, although necessary in order to allow the acceptance of the proposed devices in such laboratories, bears the disadvantage, that the substrate modes are not longer absorbed by the micropillar but are allowed to propagate and reach the output fiber-optics together with the light interacting with the cell-layer.

5.6.2 TEOS on glass

In order to transfer the H-SLLP/TEOS-on-silicon technology to a transparent substrate compatible with inverted microscopes, Pyrex glass substrates were acquired and used. In this context, the DRIE process was replaced by wet etching. The final appearance of the TEOSon-glass PhLoC shown in Fig. 5.24 is identical to its silicon counterpart, save for the transparency of the substrate.

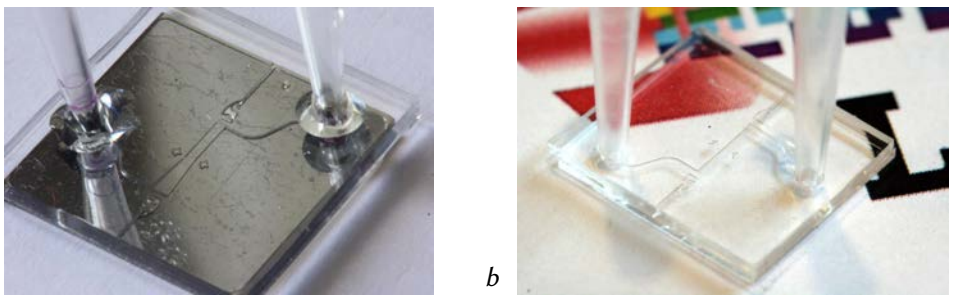

FIGURE 5.24: (a) TEOS-on-glass: Planar PhLoC design scheme comprising TEOS coated micropillar for vertical alignment. (b) TEOS-on-glass: Planar PhLoC design scheme comprising glass substrate and engraving for embedding of fiber-optics.

5.6.3 Setup for optical measurements

A miniaturized optical bench specifically designed for the PhLoC configuration is shown in Fig. 5.25

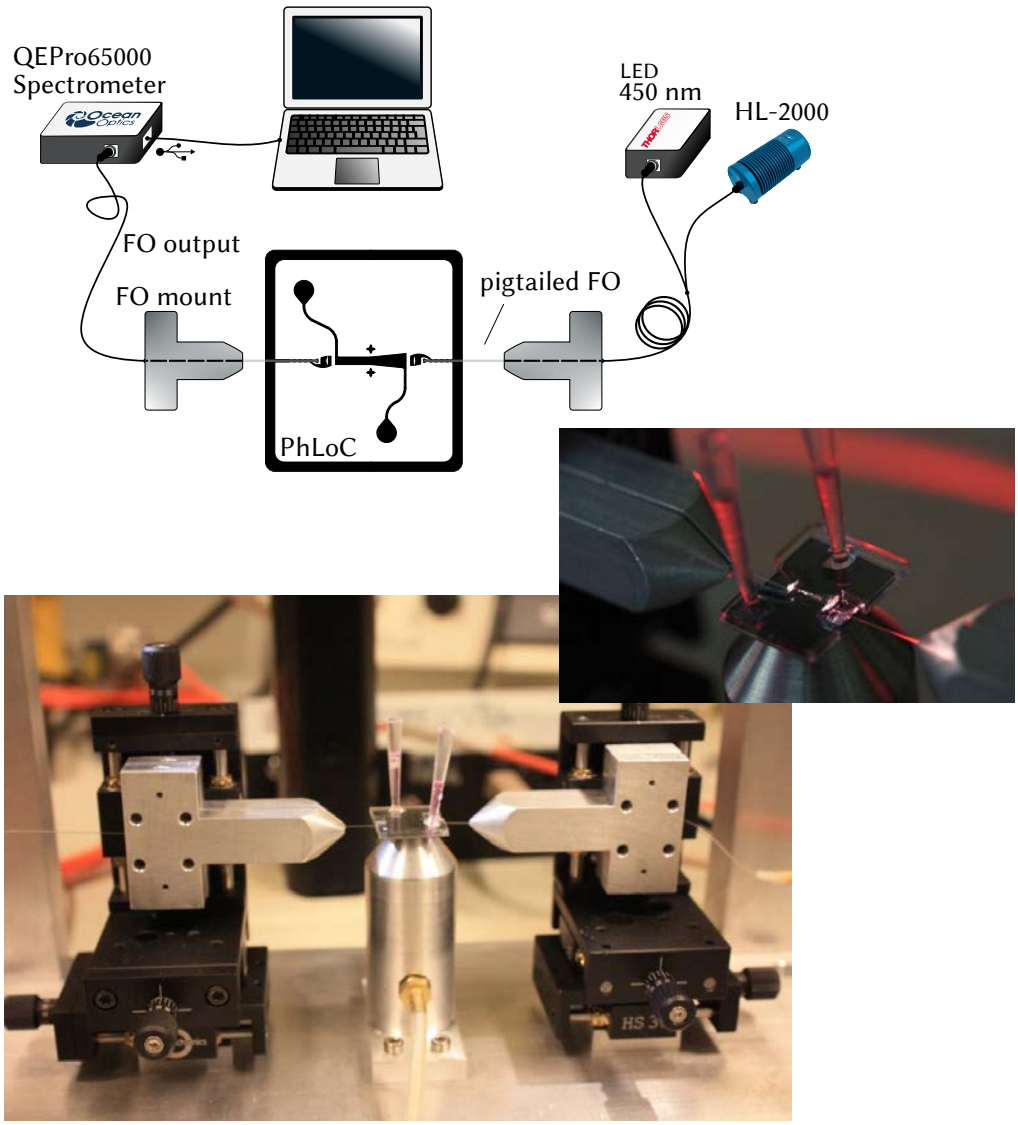

Figure 5.25: Setup for alignment of fiber-optics and PhLoC. consisting of twin 3-axis fibre optic micropositioners, a custom-made, magnetically actuated aluminium piece for fibre clamping and a vacuum-assisted centre pillar for positioning the chip. The whole system is approximately 20 x 10 cm; Inset: Detailed view of theTEOS-on-silicon PhLoC with the light coupled in.

5.6.4 TEOS-on-silicon: VSMCs

Cell culture and data acquisition. Primary VSMCs isolated from the left anterior descending coronary artery of pigs cultured in culture flasks were dissociated by trypsination and seeded in the TEOS chips which had been covered with fibronectin 24h before as shown in Fig. ??.

Using the a planar PhLoC with 2.5 mm optical path-length, healthy cells as a control culture were compared with cells perfused with TNF-α (100 ng/mol) over 19 hours. Control slides with only perfused medium were used as a reference in order to be able to remove the signal originating from the medium from the spectral response. TNF-α is known to affect calcium handling and lower global calcium in VSMCs. Therefore, by the end of the experiments, the VSMC culture was incubated with ionomycin to restore intracellular calcium, and the final spectra were measured. Ionomycin induces holes in the cell membrane, hence elevating intracellular calcium to maximal level. Spectra were taken every 2 hours from both PhLoCs.

Results. The results of the time evolution of the spectral response are summarized in Fig. 5.26 As can be seen, from the initial spectral response after 24 hours, the absorbance decreases after 2 hours of cell culture, and it remains constant for the following 19 hours (variance in the absorbance can be associated with small misalignment due to optical fibre positioning). It is important to notice that in the control, the band around 744 nm is visible right from the start of the measurements. After ionomycin inoculation, the spectra dramatically change, with an additional band located at 561 nm, close to the Phenol Red band centred at 552 nm, a shift of the 744 band, now being at 701 nm and the sharpening of the band located at 464 nm. In the spectral response of the TNF-α perfused cells, just after the injection, the characteristic band at 744 nm was not measurable, the 464 band had become much weaker, and a large band centred at 650 nm was observed. After ionomycin inoculation, the spectra also suffered a strong variation. The band at 464 nm was fully recovered, the 650 nm band showed a significant increase of its intensity, with 2-3 sub-bands (the most notable centred at 681 nm), and a dramatic decrease of the absorbance for wavelength values higher than 725 nm.

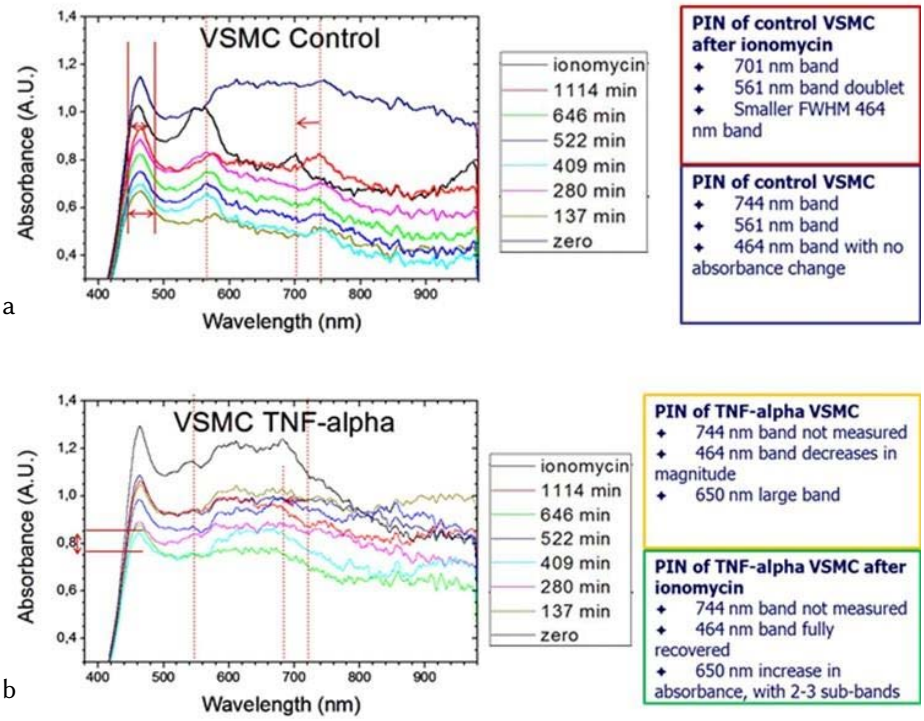

Figure 5.26: (a) (Left) Spectral response of the 2.5 mm TEOS-on-silicon in the initial state (zero), at different times. This was used as control. After 19h, ionomycin was inoculated; (Right) Summary of the characteristic absorbance bands. (b) (Left) Spectral response of the 2.5 mm TEOS-on-silicon in the initial state (zero), at different times after injecting 100 ng/mL TNF-α, and after inoculating ionomycin; (Right) Summary of the characteristic absorbance bands.

.

5.6.5 TEOS-on-glass: EA.hy962

Cell culture and data acquisition.

Twelve chips were coated with fibronectin and placed in the refrigerator overnight in a sterile chamber. A reference spectrum was recorded in each chip with culture medium in the channel before the cells were seeded. EA.hy962 endothelial cells were isolated from rat aorta and then washed three times with 5 mL PBS and trypsinated with 1 ml of trypsin. After that they were returned to the incubator until they detached (max 4 minutes). Trypsin was stopped with at least 2 mL of culture medium and cells are centrifuged for 10 minutes at 1000 rpm. Subsequently, all supernatant was removed and cells were re-suspended in 100 µL (or 200 µL).
Cells were seeded by placing the cell suspension in the pipette on one side and suck liquid from the other side of the channel to make the cells enter the chip. After that, the chips were returned to the incubator until the next day to allow the cells to attach to the channel bottom.
At this point, *with the cells attached and before changing the culture medium*, the effective reference spectrum was acquired from each chip (time $t = 0$). Fig. 5.27 shows two examples from the µ-channel of TEOS-on-glass PhLoC at time $t = 0$

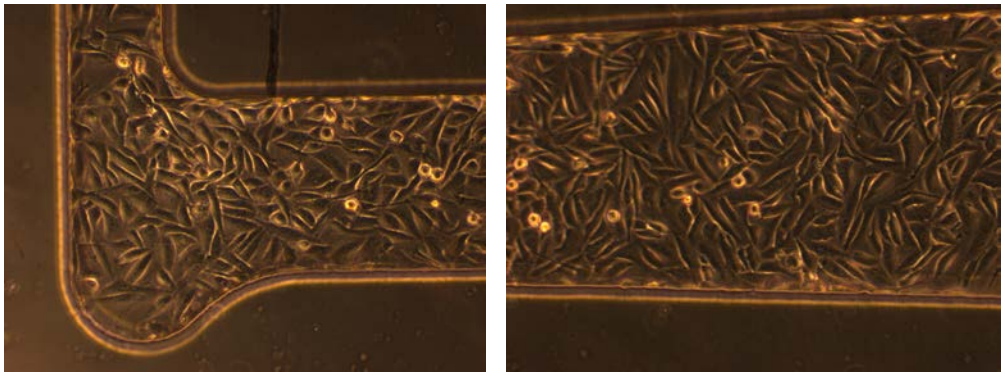

Figure 5.27: EA.hy962 cells after 24 h of culture. ($t = 0$).

Subsequently the culture medium was replaced in all of the chips and TNFα (10 ng/mL) added to half of them.
The spectral response was monitored by acquiring spectra at 1, 2, 4, 24 and 48 hours. To finish the experiments, ionomycin (10 µM) was added to the cultures and final spectra acquired.

Results and Discussion.

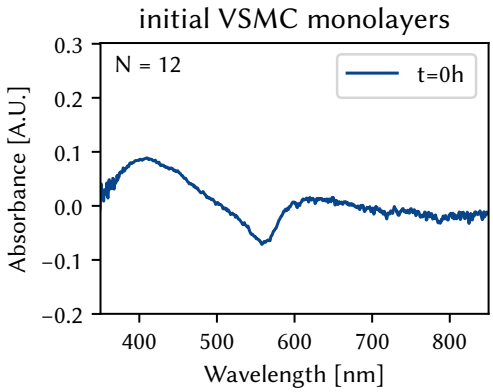

Figure 5.28: Averaged and baseline-corrected initial absorbance spectrum of VSMC monolayer.

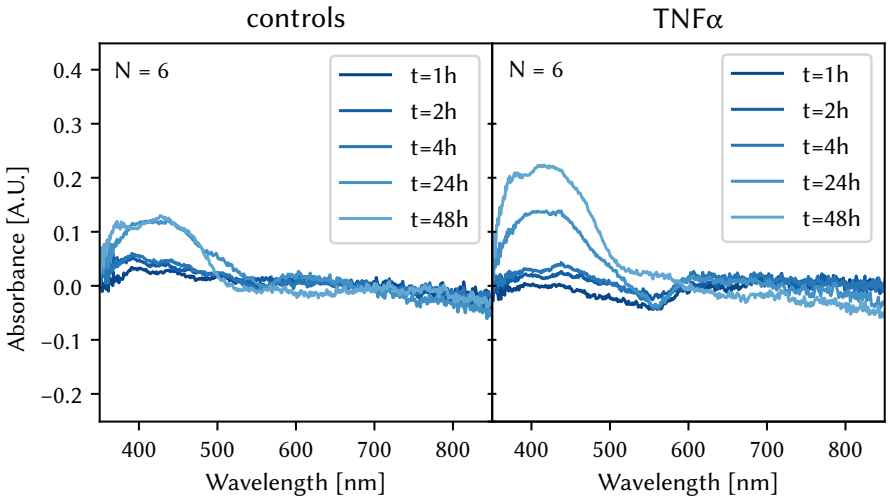

Figure 5.29: Averaged and baseline-corrected spectra over time.

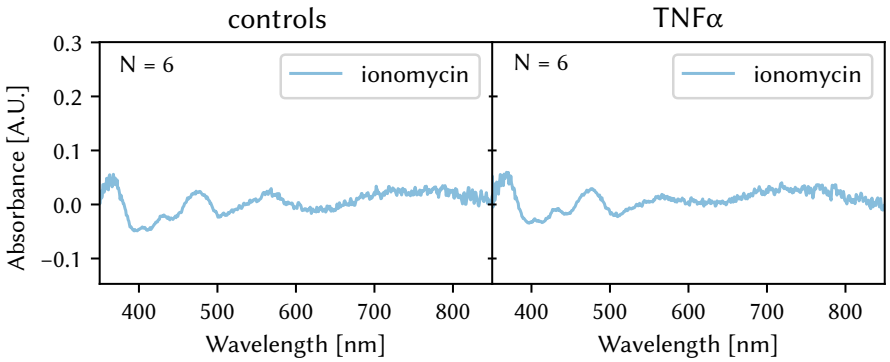

Figure 5.30: Averaged and baseline-corrected spectra after ionomycin addition.

5.7 Conclusions and outlook

In future work, waveguides should be integrated directly in order to keep the incoming light above the low-RI layer from the start. Influence of mode coupling to the underlying Pyrex has to be further investigated. Reduce uncertainty factors other than those already arising from the cells, ideally combine the PhLoC with the proposed Chip-to-world interface for monitoring inside of the incubator and avoiding repeated manual alignment and the inherent human error in such procedures.

General Conclusions and Perspective 6

As already stated in the beginning of this thesis, the implementation of living photonic elements presented a very multifaceted challenge. Our contributions regarding essential optical interfacing were focussed on robust and standardised optical connections to and from a PhLoC using a low-cost fast prototyping approach based on CO_2-laser processing. In this context, we presented a cheap, robust and easy-to-use chip-to-world interface for photonic lab-on-a-chip devices (PhLoCs). Comparing the proposed plug-optics SMA fiber-connections by themselves to a commercial fiber-to-fiber connector, we found that the performance was not significantly different. This standardization gives great versatility to the interface, providing a direct link between PhLoCs and a wide range of light sources and photo-detectors.

Experimental evaluation of the fully assembled CWI showed that the introduction of bends in the photonic structure allowed to efficiently discard stray-light artefacts and obtain a clean signal with good signal-to-noise ratio (SNR = 50). In this optimized configuration it could be shown that alignment margins of ±20 suffice to fully compensate misalignments induced by fabrication or assembly. Even through different cycles of fabrication and assembly as well as plugging in and out of the PhLoC, coupling to SU-8 multimode waveguides as thin as 6 µm has been demonstrated without significant signal variation.

The fact that PhLoCs can be easily plugged in and out by a user without a special skill-set while obtaining full functionality is a big step forward in terms of user-friendliness and potentially brings PhLoCs one step closer towards practical applications. In addition, we have demonstrated that Python is a real alternative to LabVIEW for laboratory programming and especially in terms of creating front ends for final applications. The cross platform and open source character of Python also opens pathways towards more portable equipment, especially in terms of the user interface. Our efforts regarding miniaturised monitoring instrumentation

of bacterial biofilms focussed on integrating photonic components in thermoplastic substrates - in particular commercial grade PMMA have been rather fruitful so far. We provided a cheap platform for the study of biofilm colonisation in water distribution systems. By locally modifying the surface in the detection zone, we achieved preferential adhesion and early optical detection of bacteria in static conditions via fiber-optics segments embedded in the modified substrates. For the implementation of prototypes resembling the flux and pressure conditions in real water distribution systems, we also explored the integration of polymeric waveguides with fluidic channels, successfully implementing novel fabrication strategies for the encapsulation of photolithographically obtained SU-8 structures in PMMA PhLoCs. Using these devices, and exploiting our positive results in terms of optical interconnects and software interface, monitoring of a circulating bacterial population suggested that bacterial surface colonisation can in such circumstances indeed be associated with a distinct spectral response over time.
In summary, we could demonstrate bacterial adhesion on such surfaces and even demonstrated a cheap method of locally enhancing the bacterial adhesion affinity in a controlled way. Preliminary optical data suggest that the spectral response of a biofilm may indeed by rather characteristic, thus diminishing the probability of false positives in monitoring.

Last, we investigated the adjustments to the PhLoC paradigm necessary regarding the implementation of much thinner mammalian cell monolayers as living photonics. Concretely, we focussed our efforts on the numerical evaluation an optimisation of light confinement in thin irregular layers in low-refractive index environments and the development of suitable strategies to couple light to such structures, taking into account the biological constrains, which were much more pronounced here as compared to biofilms. To that end, different materials were studied in terms of compatibility with the established material parameters, available microfabrication techniques and bio-compatibility. Finally, based on the results regarding suitable materials, we applied two of the resulting PhLoC architectures to *in vitro* cell cultures in different stages of inflammatory processes.